

RADIO CONTINUUM SURVEY OF AN OPTICALLY-SELECTED SAMPLE OF NEARBY SEYFERT GALAXIES

LUIS C. HO

The Observatories of the Carnegie Institution of Washington, 813 Santa Barbara St., Pasadena, CA 91101-1292; lho@ociw.edu

AND

JAMES S. ULVESTAD

National Radio Astronomy Observatory, P. O. Box 0, 1003 Lopezville Road, Socorro, NM 87801; julvesta@nrao.edu

To Appear in The Astrophysical Journal Supplements

ABSTRACT

We have used the Very Large Array (VLA) to conduct a survey for radio continuum emission in the sample of 52 Seyfert nuclei selected from the optical spectroscopic galaxy catalog of Ho, Filippenko, and Sargent. This Seyfert sample is the most complete and least biased available, and, as such, it will be useful for a variety of statistical analyses. Here we present the observations, measurements, and an atlas of radio maps.

The observations were made at 6 cm in the B-array and at 20 cm in the A-array, yielding matched angular resolutions of $\sim 1''$. We detected 44 objects (85%) at 6 cm and 37 objects (71%) at 20 cm above a 3σ threshold of $0.12 \text{ mJy beam}^{-1}$. The sources have a wide range of radio powers ($P \approx 10^{18}\text{--}10^{25} \text{ W Hz}^{-1}$), spectral indices ($\alpha_6^{20} \approx +0.5$ to -1), and linear sizes ($L \approx \text{few tens pc} - 15 \text{ kpc}$). The morphology of the radio emission is predominantly that of a compact core, either unresolved or slightly resolved, occasionally accompanied by elongated, jet-like features. Linearly-polarized emission was detected at 6 cm in 12 sources, 9 of which were also detected at 20 cm.

Subject headings: galaxies: active — galaxies: jets — galaxies: nuclei — galaxies: Seyfert — galaxies: structure — radio continuum: galaxies

1. INTRODUCTION

Radio emission is one of the most distinctive attributes of the active galactic nucleus (AGN) phenomenon. It varies widely in intrinsic strength and in outward appearance, ranging from the conspicuous large-scale jets in powerful radio galaxies (Fanaroff & Riley 1974), to the less energetic radio outflows seen in Seyfert galaxies (e.g., Ulvestad & Wilson 1989), to the more mundane compact, radio cores commonly found in elliptical (Sadler, Jenkins, & Kotanyi 1989; Wrobel & Heeschen 1991; Slee et al. 1994) and spiral nuclei (van der Hulst, Crane, & Keel 1981; Sadler et al. 1995).

Aside from its ubiquity among AGNs, radio continuum emission effectively traces nuclear activity because it is impervious to effects which complicate observations at shorter wavebands, namely dust obscuration in the ultraviolet, optical, and even near-infrared (IR) wavelengths, and photoelectric absorption at X-ray energies. Modern radio interferometers, moreover, can routinely and efficiently deliver sensitive, high-angular resolution maps, making them particularly attractive instruments to survey large samples of objects. During the past 25 years, radio continuum surveys have contributed fruitfully to our understanding of AGNs, especially of more nearby objects such as Seyfert galaxies. Among other things, these studies have elucidated the pervasiveness of jet-like outflows in AGNs with a wide span of intrinsic power; they have delineated the gross morphology and fine structures of nuclear regions on scales from $\sim 1\text{--}10^3 \text{ pc}$; they have highlighted the intricate interplay between the radio-emitting plasma and the

dynamics and energetics of the optical emission-line regions; and they have exploited the directional information furnished by the radio jets to make inferences on the orientation of the accretion disk. Discussions of some of these developments have been given by Wilson (1997), Bicknell et al. (1998), and Kinney et al. (2000), among others.

Many AGN investigations are statistical in nature. Some issues raised by previous radio studies of Seyfert galaxies include: (1) determination of their radio luminosity functions (Meurs & Wilson 1984; Edelson 1987; Ulvestad & Wilson 1989; Rush, Malkan, & Edelson 1996); (2) comparison between the radio properties of subtypes of Seyferts in the context of predictions from evolutionary or unification models (de Bruyn & Wilson 1978; Meurs & Wilson 1984; Edelson 1987; Ulvestad & Wilson 1984a, 1984b, 1989; Ulvestad 1986; Giuricin et al. 1990; Ulvestad, Antonucci, & Goodrich 1995; Kukula et al. 1995; Morganti et al. 1999; Nagar et al. 1999); and (3) comparison between the radio properties of Seyferts and other classes of emission-line nuclei (Heckman et al. 1983; Keel 1984; Giuricin, Mardirossian, & Mezzetti 1988; Sadler et al. 1995). The fidelity of the conclusions of such studies often is limited not by sample size — by now substantial numbers of Seyferts have been imaged at radio wavelengths — but by more subtle selection effects inherent in most, perhaps all, samples of Seyfert galaxies.

In an effort to circumvent some of these difficulties, we have undertaken a new radio continuum survey of an optically selected sample of 52 nearby Seyfert galaxies using

the Very Large Array (VLA)¹. The merits of our new sample, derived from a recently completed, extensive optical spectroscopic survey of nearby galaxies, are described in Section 2; a comparison of our sample with other major extant surveys is given in Appendix A. Details of the observations, calibrations, and data reductions can be found in Section 3. Section 4 presents maps of all the galaxies and summarizes the principal source parameters in tabular form, including optical data pertinent to subsequent analysis, which will be given in a separate paper by Ulvestad & Ho (2001). A description of the radio properties of each individual object is deferred to Appendix B. Some general statistical results of the survey are noted in Section 5.

2. THE PALOMAR SEYFERT SAMPLE

The sample of Seyfert galaxies in this paper is derived from the Palomar optical spectroscopic survey of nearby galaxies (Ho, Filippenko, & Sargent 1995). In brief, the Palomar 200-inch telescope was employed to take moderate-dispersion, high-quality spectra of 486 bright ($B_T \leq 12.5$ mag), northern ($\delta > 0^\circ$) galaxies selected from the Revised Shapley-Ames Catalog of Bright Galaxies (Sandage & Tammann 1981), with the primary aim of conducting an accurate census of the AGN population in the nearby ($z \approx 0$) universe. The Palomar survey, the most sensitive of its kind (see Ho 1996 for a comparison with previous optical studies), produced a comprehensive, homogeneous catalog of spectral classifications of nearby galaxies (Ho et al. 1997a, 1997c). The median distance² of the sample galaxies is 20.4 Mpc, with an interquartile range of 10.4 Mpc. The completeness of the Palomar survey follows that of the Revised Shapley-Ames Catalog, which, for high-surface brightness galaxies, is complete to $B_T = 12.0$ mag and 80% complete to $B_T = 12.5$ mag (Sandage, Tammann, & Yahil 1979). A significant fraction of the survey galaxies have been classified as AGNs or AGN candidates (Ho et al. 1997b) — 20% LINERs, 13% LINER/H II “transition objects,” and 11% Seyferts. The 52 Seyferts (Table 1), the subject of this paper, contain many familiar, bright objects, but there are also many which are not well known, which are not usually regarded as “active,” or whose classification has been revised.

The spectroscopic classification system is described at length in Ho et al. (1997a). Emission-line nuclei fall into one of two categories, H II nuclei (powered by stars) and AGNs (powered by black-hole accretion), according to the relative strength of the low-ionization optical forbidden lines ([O I] $\lambda\lambda 6300, 6364$, [N II] $\lambda\lambda 6548, 6583$, [S II] $\lambda\lambda 6716, 6731$) compared to the hydrogen Balmer lines. The ionization state of the narrow-line gas in AGNs, as measured through the ratio [O III] $\lambda 5007/H\beta$, distinguishes LINERs ([O III]/ $H\beta < 3$) from Seyferts ([O III]/ $H\beta \geq 3$). Finally, the presence or absence of kinematically distinct broad (linewidths ranging from one to several thousand km s^{-1}) permitted lines separates AGNs into the “type 1” and “type 2” varieties, respectively, while the relative strength of the broad component of the hydrogen Balmer lines further splits the type 1 objects into finer subdivisions (type 1.0, 1.2, 1.5, 1.8 and 1.9; see Osterbrock

1981).

Table 1 (col. 2) lists the classifications of the 52 Seyferts in our sample. It includes, in addition, two objects (NGC 4203 and NGC 4450) classified as LINER 1.9 sources by Ho et al. (1997a) which were observed as part of our program for different reasons. We present their data here for completeness, but we will exclude them from further analysis. Three additional objects (NGC 1068, 1358, and 1667) do not meet the formal definition of the Palomar sample because of their southern declination. These galaxies are included in the complete statistical analysis. The symbols have the following meaning: L = LINER, T = “transition object” (LINER + H II nucleus), and S = Seyfert. Classifications deemed to be uncertain or highly uncertain are followed by a single and double colon, respectively. In a few cases the classification assignment is ambiguous, and more than one is given, with the adopted classification listed first. NGC 4579, for example, falls near the somewhat arbitrary boundary between a Seyfert and a LINER, but because it is officially on the Seyfert side, it is classified as “S1.9/L1.9”; the “1.9” designation means that broad $H\alpha$, but not broad $H\beta$, has been detected. There are 30 type 2 and 22 type 1 objects.

The rest of the entries in Table 1 are as follows: col. (3) Hubble type; col. (4) morphological type index (T); col. (5) total apparent B magnitude of the galaxy (B_T); col. (6) adopted distance (D); cols. (7) and (8) optical position in epoch J2000. Data for cols. (2)–(6) are taken from the compilation of Ho et al. (1997a). The optical positions with sub-arcsecond accuracy come from Clements (1981, 1983) and Argyle & Eldridge (1990), and the rest are taken from Cotton, Condon, & Arbizzani (1999).

Because of the proximity of the objects (median $D = 20.4$ Mpc; Fig. 1a) and the sensitivity of the Palomar survey to weak emission lines, it is not surprising that our sample contains a significant number of low-luminosity sources. Figure 1d shows the distribution of extinction-corrected luminosities for the narrow component of the $H\alpha$ line; with the exception of the possibly anomalous object NGC 185 (see Appendix B), $L(H\alpha)$ ranges from $\sim 1 \times 10^{38}$ to $3 \times 10^{41} \text{ erg s}^{-1}$, with a median value of $5 \times 10^{39} \text{ erg s}^{-1}$. By contrast, Markarian Seyferts have typical $L(H\alpha) \approx 10^{40} - 10^{42} \text{ erg s}^{-1}$ (Dahari & De Robertis 1988). Among “classical” Seyferts, NGC 4051 holds the record for having the lowest optical continuum luminosity ($M_B = -16$ mag, adjusted to $H_0 = 75 \text{ km s}^{-1} \text{ Mpc}^{-1}$; Véron 1979), and in previous surveys, the optical luminosity function of Seyferts does not extend fainter than $M_B \approx -18$ mag (e.g., Huchra & Burg 1992). Although nuclear continuum magnitudes are not yet available for all the objects in our sample, a few examples are illustrative: NGC 3031 ($M_B = -11.6$ mag; Ho, Filippenko, & Sargent 1996); NGC 4395 ($M_B = -9.8$ mag; Filippenko, Ho, & Sargent 1993); NGC 4579 ($M_B = -11.8$ mag; Barth et al. 1996); NGC 4639 ($M_B = -12.5$ mag; Ho et al. 1999a). The host galaxies, on the other hand, are generally luminous (median $M_{B_T}^0 = -20.7$ mag; Fig. 1b), bulge-dominated (median $T = 2.0$, or Hubble type Sab; Fig. 1c) galaxies.

The Palomar sample of Seyferts has several merits com-

¹The VLA is operated by the National Radio Astronomy Observatory, a facility of the National Science Foundation operated under cooperative agreement by Associated Universities, Inc.

²In this and subsequent papers, we adopt the distance estimates of Tully (1988), who assumes a Hubble constant of $H_0 = 75 \text{ km s}^{-1} \text{ Mpc}^{-1}$.

pared to other samples (see Appendix A). First, as an optically selected sample with complete spectroscopic identification, it is less susceptible to strong biases as in the samples selected in the ultraviolet or IR. (See § A.2 for a discussion of selection biases in Seyfert samples.) Unlike other optically selected samples, such as that extracted from the CfA redshift survey (Huchra & Burg 1992) or from heterogeneous literature compilations (Maiolino & Rieke 1995), the Palomar Seyferts are derived from a survey with uniform, high-quality data, classified with well defined and objective criteria. Particular care was taken to account for the severe contamination of the nuclear signal by the starlight of the host galaxy. Second, the close distances of the objects offer a number of advantages. In addition to maximizing the achievable linear resolution and signal-to-noise ratio (S/N), the relative proximity of the galaxies enhances the contrast between the nucleus and the bright, surrounding bulge of the host galaxy. This is a crucial factor in detecting weak nuclei. Third, our sample covers a large range of AGN luminosities, making it ideal for exploring possible trends with AGN power. Fourth, the parent Palomar survey is sufficiently large that it contains all nuclear spectral classes and accurate statistical representation of each class, and so comparative analyses among different subsamples can be done in a straightforward manner. Finally, the Palomar objects are currently the focus of several other studies, thus ensuring the availability of a rich database for multiwavelength investigations.

3. OBSERVATIONS AND DATA REDUCTIONS

We observed the galaxies during two sessions using the VLA (see Table 2 for a summary). On 1999 August 29, while the array was in its A-configuration (Thompson et al. 1980), observations were acquired at a central sky frequency of 1.425 GHz (L band; 20 cm). Matched-array data were taken with the B-configuration at 4.860 GHz (C band; 6 cm) on 1999 October 31. The weather conditions were excellent during both observing sessions. To achieve maximum sensitivity, we used both intermediate frequencies, each of width 50 MHz, separated by 50 MHz. Since we are mainly concerned with the emission from the nucleus, which was placed at the phase-tracking center, bandwidth smearing (Bridle & Schwab 1999) is not a problem despite the somewhat large bandwidth. The excellent sensitivity of the current 6 and 20 cm receivers of the VLA routinely permits high S/N maps to be made in relatively short integration times. Each target was observed for 15–18 min, immediately preceded and followed by a short (~ 3 min) exposure of a nearby phase calibrator to calibrate the antenna gains and phases. More than half the phase calibrators used have position accuracies of $0''.01$ or better, either from VLBI observations (Ma et al. 1998; Eubanks et al. 1998) or from VLA observations (Patnaik et al. 1992; Browne et al. 1998); the rest of the calibrators have position accuracies of $\sim 0''.1$ (Wilkinson et al. 1998; VLA staff, unpublished). The self-calibration typically moved source positions by less than $0''.01$, indicating that atmospheric phase irregularities had a relatively small effect on source positions. Therefore, in most cases, the measured positions are accurate to $0''.1$ or better. For a few very weak sources, the position can only be determined with an ac-

curacy of approximately the beam size divided by the S/N of the detection, which can be as large as $0''.3$ for a $5\text{-}\sigma$ detection. We tied the absolute fluxes to the VLA scale by observing 3C 286, whose flux densities at 6 and 20 cm were assumed to be 7.49 and 14.75 Jy³, respectively. Errors in the quoted flux densities are dominated by the uncertainty in setting the absolute flux scale, conservatively estimated to be 5%.

Antenna polarization leakage was calibrated by observing the calibrator 1313+675 through a wide range of parallactic angles. The complex instrumental polarization of the antennas, determined to an accuracy of $\sim 0.2\%$, was removed from the cross-polarized visibility data, and the right and left circularly-polarized channels were aligned by assuming that the position angle (P.A.) of the electric vector of 3C 286 was $+33^\circ$ at both 6 and 20 cm.

Two of the galaxies in our sample (NGC 3031 and NGC 7743) were observed with wrong coordinates and were missed. Fortunately, both sources have been observed previously with the VLA in setups similar to that of our program, and we were able to retrieve their data from the archives and reprocess them in a way consistent with our own observations. The NGC 3031 data were originally published by Kaufman et al. (1996), while the NGC 7743 data were published by Wrobel & Heeschen (1991) and Nagar et al. (1999). For NGC 7743, the 6 cm data set comes from the C-configuration, since the only existing B-configuration data also were obtained with an incorrect position.

After editing and calibration, the visibilities were Fourier transformed into maps of sky brightness using the algorithm IMAGR in AIPS (van Moorsel, Kemball, & Greisen 1996). The sidelobes of the synthesized beam were removed from the “dirty” maps by applying the deconvolution “CLEAN” procedure of Högbom (1974), as modified by Clark (1980), to “clean boxes” placed around sources stronger than ~ 0.5 mJy within the primary-beam area. The number of iterations was set so that the minimum “clean component” reached 0.12 mJy beam⁻¹, ~ 3 times the theoretical thermal noise limit of the maps. We constructed images at different resolutions by applying appropriate tapering functions to the visibilities. Three sets of total-intensity (Stokes I) maps were made, at full resolution and with Gaussian tapering functions falling to 30% at 80 and 50 k λ ; these correspond to synthesized beams of $\Delta\theta \approx 1''.1$, $2''.5$, and $3''.6$, respectively. The untapered maps were “uniformly weighted” to yield the highest angular resolution, at the expense of a slight degradation in sensitivity. The tapered maps, “naturally weighted” for maximum sensitivity, have dimensions comparable to the half-power beam width (HPBW) of the antenna primary beam ($8''.4$ at 6 cm, $28''.1$ at 20 cm). They were used to assess the possible presence of extended emission and to evaluate whether sources far from the map center might be introducing sidelobe contamination near the nucleus. In our chosen configurations and frequencies, the shortest u - v spacings are ~ 3 k λ , and so our images are sensitive only to structures with angular scale $\lesssim 1''$.

The theoretical root-mean square (rms) noise of our snapshot images is expected to be ~ 0.04 mJy beam⁻¹, a level attained in most of the maps where sidelobe con-

³1 Jy = 10^{-23} erg s⁻¹ cm⁻² Hz⁻¹.

tamination, either from the nucleus itself or from nearby background sources, was not severe. For sources with sufficiently high S/N, the dynamic range of interferometer maps can be further improved through self-calibration to remove antenna-based phase and amplitude errors (Cornwell & Fomalont 1999). Using the initially deconvolved maps as input models to the CALIB algorithm, the S/N of a number of objects improved dramatically after application of several cycles of self-calibration. In a few cases a strong background source within the primary-beam area was used as the model. For NGC 1167 and NGC 1275, the radio emission was strong enough that the dynamic range was still limited, probably by baseline-based errors. Correcting such errors by self-calibration significantly improved the NGC 1167 images, but had little effect on NGC 1275.

In addition to the total-intensity images, we also made full-resolution, naturally-weighted maps of the Stokes Q and U intensities, combinations of which resulted in maps of the amplitude, $I_{\text{pol}} \equiv \sqrt{Q^2 + U^2}$, and the electric vector P.A., $\chi \equiv 1/2 \tan^{-1}(U/Q)$ of the linearly-polarized intensity. The typical rms noise of the I_{pol} maps is ~ 0.025 mJy beam $^{-1}$. The 3σ detection threshold, after correcting for the known positive bias of I_{pol} (e.g., Wardle & Kronberg 1974), is ~ 0.079 mJy beam $^{-1}$. However, owing to linear approximations in the treatment of polarization impurities in the feeds, there is also a lower limit of $\sim 0.2\%$ in detectable polarization fraction. This limit is higher than the nominal detection threshold for components with peak intensities greater than ~ 40 mJy beam $^{-1}$.

4. MAPS AND SOURCE PARAMETERS

We present the survey data as a series of greyscale images superposed with contours. The two representations emphasize different details. The maps for all 54 objects, including eight nondetections, are shown in Figures 2–15. Each figure (except Fig. 15) displays four galaxies, arranged in the order of increasing NGC number. For each galaxy, the left panel (*a*) shows the full-resolution, uniformly-weighted 20 cm map, the middle panel (*b*) shows the full-resolution, uniformly-weighted 6 cm map, and the right panel (*c*) shows the naturally-weighted, tapered 6 cm map. Panels (*a*) and (*b*) are registered, both with identical dimensions, which in nearly all cases are $30'' \times 30''$. The resolution of the tapered maps is either $\Delta\theta \approx 2''.5$ or $3''.6$, depending on which better illustrates the extended emission, and the dimensions of some plots have been optimized to display particular features in each galaxy.

The restoring beam (identical for the two full-resolution panels) is depicted as a hatched ellipse on the lower left-hand corner of each map. The contour levels of the maps are $\text{rms} \times (-6, -3, 3, 6, 12, 24, 48, \dots)$, where the rms values for the maps are given in Table 3. The optical position of the galaxy is marked with a cross, the semi-major length of which corresponds to the uncertainties given in Table 1. Note that the cross symbol is not visible on the scale of these maps for objects whose optical positions have sub-arcsecond accuracy.

We have adopted a consistent method in extracting source parameters. The rms noise of each map is determined from a source-free, rectangular region. The galaxy is considered detected if a source with a peak flux den-

sity $S^P \geq 3 \times \text{rms}$ is found within the error box of the optical position given in Table 1. For undetected sources, the upper limit is set to $S^P < 3 \times \text{rms}$. Whenever possible we determined the source parameters (position, peak flux density, integrated flux density, deconvolved source dimensions, and P.A.) by fitting a two-dimensional Gaussian model using the task JMFIT. The P.A. is measured from North through East, from 0° to 180° . This procedure works well for sources with relatively simple, symmetric structure, such as most galaxy cores. For components with more complex morphologies, or for weak, marginal detections, we simply integrated the signal within inter-actively defined boundaries (using the task IMEAN for rectangular boxes and TVSTAT for irregularly shaped regions). In these instances the highest pixel value defined the peak flux density and its position, and the source size and P.A. were estimated manually on the image display. A source is considered resolved if its deconvolved size is larger than one-half the beam size at full width at half maximum (FWHM) in at least one of the two dimensions. Upper limits to the sizes of unresolved sources are set to one-half the beam size at FWHM.

Two sets of measurements are given for each galaxy, one based on the high-resolution, uniformly-weighted map, the other on the tapered map. In addition to a central core, some objects show obvious additional complex structure such as a circumnuclear ring (e.g., NGC 1068 and NGC 6951), jet-like extensions (e.g., NGC 1358, 3031, 3516, 4388, 5033), and other amorphous protrusions (e.g., NGC 3079). If a meaningful decomposition of the components could be made, they were measured separately on the high-resolution map.

Linear polarization was detected at 6 cm for 12 objects, of which 9 were also detected at 20 cm (see § 5). These objects are shown in greater detail in Figure 16. The contours show maps of total intensity, as in Figures 2–15, and superposed are vectors representing linearly-polarized emission.

The measured quantities are collected in Table 3. Multiple entries for the high-resolution map denote different components; if warranted, we generally give separate measurements for the entire source as well as for the central “core” alone. The columns are as follows: col. (1) galaxy name; col. (2) figure number for maps; col. (3) FWHM of the elliptical Gaussian restoring beam; col. (4) P.A. of the restoring beam; cols. (5) and (6) rms noise of the 6 cm and 20 cm maps; cols. (7) and (8) radio position in epoch J2000; col. (9) peak flux density at 6 cm (S_6^P); col. (10) integrated flux density at 6 cm (S_6^I); col. (11) peak flux density at 20 cm (S_{20}^P); col. (12) integrated flux density at 20 cm (S_{20}^I); col. (13) spectral index between 6 and 20 cm (α_6^{20}) defined such that $S_\nu^I \propto \nu^{\alpha}$, where S_ν^I is the integrated flux density at frequency ν ; col. (14) deconvolved FWHM dimensions (major \times minor axis, $\theta_M \times \theta_m$) of the fitted source, determined from an elliptical Gaussian fit; col. (15) P.A. of the fitted source; col. (16) peak linearly-polarized flux density at 6 cm ($S_{\text{pol},6}^P$); and col. (17) peak linearly-polarized flux density at 20 cm ($S_{\text{pol},20}^P$). Additional information on individual galaxies, including comparisons with published data, is given in Appendix B.

We have not assigned formal error bars to the radio measurements, but here we give a brief assessment of their

magnitude.

1. The radio positions for the fitted components have a nominal accuracy of $0''.1$, which is dominated by the astrometric accuracy of the phase calibrators. Positions based on identification of the highest peak are expected to have lower accuracy, on the order $\sim 0''.1$ – $0''.5$ (see § 3). Our judgement of the accuracy of the positions is reflected in the number of significant digits shown in columns 7 and 8 in Table 3.
2. Although formal errors for the source structural parameters (θ_M , θ_m , and P.A.) can be evaluated for the elliptical Gaussian fits (e.g., Condon 1997), the true errors are likely to be mainly systematic in nature, depending on whether the source can be well represented by the model.
3. The uncertainty on the flux densities can be taken to be $\sigma_S \approx \sqrt{Nrms^2 + (0.05S)^2}$, the quadrature sum of the rms noise covered by a source occupying N beam areas and a nominal 5% uncertainty on the absolute flux-density scale (e.g., Weiler et al. 1986). An unresolved source with a flux density of 1 mJy typically has $\sigma_S \approx 0.06$ mJy.
4. The fidelity of spectral-index measurements depends critically on the geometry of the source and the u - v coverage at the two frequencies. We have attempted to minimize systematic uncertainties by observing our sample using scaled arrays. Our spectral-index calculations are based on maps made using identical mapping parameters, and we have restored the cleaned 20 cm maps using the synthesized beam determined from the 6 cm maps. Nonetheless, our snapshot observations are not expected to yield exactly the same u - v coverages at 6 and 20 cm, especially for objects at very northerly declinations whose beam is highly noncircular. (Of course, the impact of differing u - v coverages is not significant for sources that are clearly unresolved.) Furthermore, three antennas were unavailable during the 20 cm observations, but all 27 were present at 6 cm. We therefore list spectral indices only for source components measured from the high-resolution (untapered) maps. The potentially dominant source of error, however, is that due to the nonsimultaneity of the observations at the two bands. Some of the sources are known to vary, on a variety of timescales. For nonvariable sources or near-simultaneous observations, the uncertainty on the spectral index formally follows from $\sigma_\alpha = \sqrt{(\sigma_6/S_6)^2 + (\sigma_{20}/S_{20})^2} / [\ln(4.8601 \text{ GHz}/1.4250 \text{ GHz})]$. For a typical 1–5 mJy source in our survey, $\sigma_\alpha \approx 0.06$ – 0.08 .

The fields of many of the objects, especially at 20 cm, contain additional detectable sources located outside of the error box of the optical position of the nucleus. The majority of these must be background sources, although we cannot rule out that a few may be associated with the galaxies themselves. For the sake of completeness, we provide in Table 4 a list of positions and integrated flux

densities for all the non-nuclear sources detected in the uniformly-weighted maps. Note that we have identified more background sources at 20 cm than at 6 cm because of the larger primary beam at 20 cm and the steep spectrum of most field sources. We have not attempted to track down the 6 cm counterparts of all the 20 cm sources. The positions are given only to an accuracy of $\sim 1''$ because the shapes of some of the sources are severely distorted (elongated) due to bandwidth smearing (see, e.g., Bridle & Schwab 1999). Whenever possible, we measure the positions from the 6 cm maps because bandwidth smearing is less severe at the higher frequency. The flux densities have not been corrected for primary-beam attenuation.

A compilation of derived radio parameters is given in Table 5, along with several optical parameters which will be used in the analysis by Ulvestad & Ho (2001). The two galaxies not in the Seyfert sample (NGC 4203 and NGC 4450) are not included in this table. The radio quantities listed are as follows: cols. (2) and (3) logarithm of the peak core (P_6^{core}) and integrated total (P_6^{tot}) power at 6 cm; cols. (4) and (5) logarithm of the peak core (P_{20}^{core}) and integrated total (P_{20}^{tot}) power at 20 cm; col. (6) largest angular size (Θ); col. (7) largest linear size (L); col. (8) P.A. of the source major axis (P.A._{rad}); and col. (9) radio morphology class. The quantities listed pertain only to the “AGN” component of the maps. The circumnuclear rings of NGC 1068 and NGC 6951, for example, have not been included in the measurements. The total integrated powers were measured from the tapered maps, if these exhibit additional emission pertinent to the AGN component which has been resolved out in the untapered maps. When determining the extent and orientation of the radio source, we examined both the tapered and untapered maps, at 6 and at 20 cm, and we adopted one final representation to make the measurements. The source size occasionally differed slightly among the maps, but in general there is good consistency. We adopt the definitions of Ulvestad & Wilson (1984a) for the radio morphology classes: “U” (single, unresolved), “S” (single, slightly resolved), “D” (diffuse), “L” (linear structure or multiply aligned components), and “A” (ambiguous). A slightly resolved source is one whose deconvolved size is $\geq 1/2$ the synthesized-beam width. When a morphological classification includes two characters, the first refers to the core and the second to the extended emission. For instance, “U+L” indicates an unresolved (U) core within a linear (L) extended source. The following optical data were taken from the catalog of Ho et al. (1997a): col. (10) total absolute B -band magnitude of the galaxy, corrected for internal extinction (M_{BT}^0) as prescribed by de Vaucouleurs et al. (1991); col. (11) P.A. of the optical major axis of the galaxy (P.A._{opt}); cols. (12) and (13) logarithm of the luminosity of the [O III] $\lambda 5007$ [L([O III])] and narrow H α [L(H α)] emission lines (erg s^{-1}), both corrected for Galactic and internal extinction; and col. (14) FWHM of the [N II] $\lambda 6583$ emission line [FWHM([N II])], which is taken as representative of the velocity dispersion of the narrow-line gas. We note that the emission-line luminosities of any individual object may have significant uncertainty, although statistical measures for the whole sample or for substantial portions thereof should be more reliable; see Ho et al. (1997a) for a detailed discussion of the limitations of the optical spec-

troscopic data.

5. GENERAL RESULTS AND SUMMARY

The optical spectroscopic survey of Ho, Filippenko, and Sargent (1995, 1997a) has yielded a new, comprehensive catalog of 52 Seyfert galaxies, the most complete and least biased available. We acquired moderately high-resolution ($\sim 1''$) 6 and 20 cm observations using the VLA to characterize the radio continuum properties of this sample. This paper presents the observational material, along with a compilation of optical parameters to be used in subsequent analyses.

We have detected the vast majority of the objects in our sample. Forty-four of the 52 Seyfert galaxies in our sample, 85%, were detected at 6 cm. The success rate at 20 cm is somewhat lower (37/52 or 71%), most likely because of the higher noise in the maps due to confusion from background sources. Eight of the sources seen at 6 cm (NGC 3185, 3941, 4169, 4378, 4477, 4639, 4698, and 5631) may be deemed marginal detections; their peak flux densities are on the order of 0.15–0.3 mJy beam $^{-1}$, or ~ 3.5 –6 times the rms noise. In nearly all cases, however, the source is present both in the untapered *and* in the tapered maps, thus lending confidence to its reality. Only two (NGC 4169 and NGC 5631) of these eight, on the other hand, were also detected at 20 cm. Although this might suggest that these weak 6 cm sources are spurious, it is possible that they escaped detection at 20 cm because of the higher systematic noise in these maps.

The sources in our sample extend to significantly lower radio powers than in many previous surveys. Figure 17 shows distributions of the core and total radio powers. The weakest source has 10^{18} W Hz $^{-1}$, the strongest $\sim 10^{25}$ W Hz $^{-1}$. The median powers for the detected sources are as follows: $P_6^{\text{core}} = 1.7 \times 10^{20}$ W Hz $^{-1}$, $P_6^{\text{tot}} = 3.5 \times 10^{20}$ W Hz $^{-1}$, $P_{20}^{\text{core}} = 4.4 \times 10^{20}$ W Hz $^{-1}$, and $P_{20}^{\text{tot}} = 9.5 \times 10^{20}$ W Hz $^{-1}$.

A wide range of morphologies is seen, but the most common is that of a single compact source centered on the position of the optical nucleus. Thirty-six of the 44 objects (82%) detected at 6 cm contain either an unresolved (23) or slightly resolved (13) central source. Among these, 14 (or 32% of all detected sources) have additional extended emission which can be considered “linear,” many reminiscent of jet-like or outflow structures. The eight marginally detected sources have simply been labeled as “ambiguous.”

A histogram of the largest linear sizes is shown in Figure 18a. They range from a few tens of parsecs for the nearest objects to ~ 15 kpc for the most distant. The mean of the distribution, computed using the Kaplan-Meier product-limit estimator (Feigelson & Nelson 1985) to account for the upper limits, is 2.1 ± 0.54 kpc.

While the extended components of the radio sources tend to have steep spectra, a nonnegligible fraction of the

cores have flat or even inverted spectra (Fig. 18b). If we define a flat-spectrum source as one with $\alpha_6^{20} \geq -0.30$, 35% (13/37) of the cores with measurable spectral indices qualify as such. The median of the distribution of α_6^{20} is -0.46 .

Finally, linearly-polarized emission was detected in 12 objects. Nine objects (NGC 1068, 1167, 2655, 3031, 4151, 4472, 5194, 5548, and 7479) were detected at 6 and 20 cm, and three (NGC 2639, 3079, and 3147) only at 6 cm. Radio polarization has been reported previously in only a small handful of Seyferts (NGC 1068, Wilson & Ulvestad 1983; NGC 3031, Kaufman et al. 1996; NGC 3079, Duric & Seaquist 1988; NGC 5194, Crane & van der Hulst 1992). Prior to this study, radio polarization has not been searched systematically in most Seyfert galaxies. Often, radio observations have been short snapshots in which no calibrator has been observed over a wide enough range of parallactic angles to calibrate the antenna polarization properties. In the present sample, the detection of polarization is limited evidently by sensitivity, since the detected sources all tend to have the highest total flux densities. Whereas the polarization detection rate is just 27% (12/44) for all the objects detected in total intensity at 6 cm, it climbs to 55% (12/22) among those with $S_6^I \geq 10$ mJy, and it reaches 89% for the nine brightest sources with $S_6^I \gtrsim 50$ mJy. With only a few exceptions, the strongest polarization signal within each source is generally *not* coincident with the galaxy core. Instead, the polarization fraction is highest in the extended components, often associated with jet-like or outflow features. Good examples can be seen in NGC 1068 (Fig. 16a), NGC 3031 (Fig. 16d), NGC 3079 (Fig. 16g), and NGC 5548 (Fig. 16k). And even in galaxies where the polarized emission is associated with a slightly resolved core, the polarization vectors seem to trace smaller scale structure directed away from the nucleus (e.g., NGC 1167, Fig. 16b; NGC 4472, Fig. 16j).

A more complete description of the statistical properties of this survey and their astrophysical implications will be given by Ulvestad & Ho (2001).

The research of L. C. H. is partly funded by NASA grant NAG 5-3556, and by NASA grants GO-06837.01-95A and AR-07527.02-96A from the Space Telescope Science Institute (operated by AURA, Inc., under NASA contract NAS5-26555). L. C. H. is grateful for travel support from the NRAO and thanks the VLA staff for their hospitality during an extended visit to Socorro in December 1999. We thank Marianne Vestergaard for helpful comments on the manuscript, and Joan Wrobel for useful discussions of polarization upper limits. This work made extensive use of the NASA/IPAC Extragalactic Database (NED) which is operated by the Jet Propulsion Laboratory, California Institute of Technology, under contract with NASA.

APPENDIX

SAMPLE CONSIDERATIONS

Previous Surveys

To fully appreciate the merits and limitations of the sample of Seyferts studied in this paper, it is useful to recapitulate the features of the main extant radio continuum surveys of Seyferts.

The Westerbork Surveys

The Westerbork Synthesis Radio Telescope (WSRT) was used to map at 20 cm a sample of ~ 75 Seyfert galaxies and related emission-line objects chosen from the first nine lists of Markarian objects. The rms noise of the maps is $\sim 1\text{--}1.3$ mJy beam $^{-1}$, and the synthesized beam is $\sim 25''$. The results of the survey are presented in de Bruyn & Wilson (1976, 1978), Meurs & Wilson (1981, 1984), and Wilson & Meurs (1982). Most of the objects are relatively distant, with $\langle D \rangle \approx 250$ Mpc, and those which were detected have typical powers of $P_{20\text{ cm}} \approx 10^{21} - 10^{24}$ W Hz $^{-1}$.

The VLA Surveys

Soon after the construction of the VLA, it was used to map in greater detail the brightest Markarian Seyferts which were detected earlier at Westerbork (Wilson & Willis 1980; Ulvestad, Wilson, & Sramek 1981; Ulvestad & Wilson 1984a). These observations were extended to include all known Seyfert galaxies observable from the VLA ($\delta \geq -45^\circ$) within $cz = 3100$ km s $^{-1}$ (the “nearby sample,” total 25 objects; Ulvestad & Wilson 1984b), and then additional objects within $cz = 4600$ km s $^{-1}$ (the “distance-limited sample,” total 57 objects; Ulvestad & Wilson 1989). The majority of the VLA observations were done at 6 and 20 cm in the A-configuration, and the resulting maps had a typical synthesized beam of $\lesssim 1''$ and an rms sensitivity of 0.1–0.2 mJy beam $^{-1}$. The latest update to this series is published by Nagar et al. (1999), who, in addition to a recessional velocity limit $cz < 7000$ km s $^{-1}$, further restricted the sample to early-type host galaxies (mostly S0s). The maps were made at 3.6 and 20 cm, with resulting beam sizes of $\sim 0''.3$ and $\sim 1''$, and rms sensitivities of 0.04–0.09 and 0.08–0.15 mJy beam $^{-1}$, respectively.

The Piccinotti et al. Sample

The *HEA0-1* A-2 all-sky survey produced a complete sample of AGNs, the majority of which are Seyferts, selected in the hard X-ray (2–10 keV) band (Piccinotti et al. 1982). The 28 sources accessible from the VLA have been detected at 6 and 20 cm with resolutions $\lesssim 1''$ (Unger et al. 1987).

The CfA Seyferts

The CfA redshift survey produced an optical magnitude-limited ($m_{pg} < 14.5$ mag) sample of 48 Seyfert galaxies (Huchra & Burg 1992). Edelson (1987) obtained observations of this sample at 1.5 cm using the Owens Valley single-dish 40 m telescope (beam $\sim 1'.5$) and at 6 and 20 cm using the VLA in its D-configuration (beam $\sim 15''$ and $45''$, respectively). The angular resolution of these data, however, was too coarse to separate the nuclear emission from the host galaxy emission, which in many cases is not insignificant.

Kukula et al. (1995) remedied this problem by reobserving the CfA sample with the VLA in the A and C-configurations at 3.6 cm, producing high-sensitivity maps (rms $\approx 0.07\text{--}0.1$ mJy beam $^{-1}$) at resolutions of $0''.3$ and $2''.5$, respectively. The CfA Seyferts have distances of 10–300 Mpc, and they emit $P_{20\text{ cm}} \approx 10^{20} - 10^{23}$ W Hz $^{-1}$.

The 12- μ m Sample

Spinoglio & Malkan (1989) constructed a galaxy catalog selected at 12 μ m from the *Infrared Astronomical Satellite* (*IRAS*) database, within which they identified a sample of AGNs based mostly on existing published optical spectroscopic classifications. The 12- μ m sample contains ~ 60 Seyferts; the radio properties of 42 of these were studied by Rush et al. (1996) using the VLA at 6 and 20 cm in the D-configuration. As in Edelson’s (1987) treatment of the CfA sample, the coarse resolution of the maps potentially confuses the nuclear regions with significant emission from the host galaxy. The 12- μ m objects have distances up to 300 Mpc, and so the coarse synthesized beams of $15''$ (6 cm) and $45''$ (20 cm) correspond to linear dimensions of 23 and 68 kpc, respectively. Thean et al. (2000) recently have obtained VLA 3.6 cm maps of the “extended” 12- μ m sample (Rush, Malkan, & Spinoglio 1993), at much higher angular resolution, at $\Delta\theta \approx 0''.3$.

The “Warm” IRAS Sample

Luminous AGNs can be identified efficiently by their far-IR colors because they tend to have flatter IR spectra (“warmer” colors) compared to normal or starburst galaxies (de Grijp et al. 1985, 1987, 1992; Osterbrock & De Robertis 1985; Kailey & Lebofsky 1988; Low et al. 1998; Keel, de Grijp, & Miley 1988). Schmitt et al. (2001) have analyzed new and archival 3.6 cm VLA A-array data for a subset of 74 nearby ($z \leq 0.031$) Seyferts from the sample of de Grijp et al. (1987, 1992).

The PTI Studies

The two-element Parkes-Tidbinbilla Interferometer (PTI) has a baseline of 275 km, which at 8.4 GHz produces a fringe spacing of $0''.03$. A set of studies have capitalized on this capability of the PTI, using it to search for compact, high-brightness temperature cores in Seyfert galaxies. Norris et al. (1988, 1990) and Roy et al. (1994) observed at 1.7 and 2.3 GHz a large sample of spiral galaxies, some of which are classified as Seyferts, selected by their *IRAS* far-IR flux. Sadler et al. (1995) extended the frequency coverage to 8.4 GHz. The rms sensitivities of the PTI data are 0.5–3 mJy beam $^{-1}$.

Others

For completeness, we mention three other related studies.

Ulvestad (1986) made VLA maps of the 10 “intermediate” type (1.8 and 1.9) Seyferts (Osterbrock 1981; Cohen 1983) known as of early 1984. The observations were done in the A and B-configurations, at 6 and 20 cm, yielding maps with resolutions of $0''.5\text{--}4''$ and rms sensitivities of $\sim 0.1\text{ mJy beam}^{-1}$.

Osterbrock & Pogge (1985) drew attention to the unusual kinematic and excitation characteristics of a subclass of objects since termed “narrow-lined Seyfert 1 galaxies.” Ulvestad et al. (1995) examined the radio properties of the 17 such objects for which optical spectropolarimetric measurements were obtained by Goodrich (1989). Their compilation includes data at 3.6, 6, and 20 cm, with resolutions ranging from $0''.2$ to $1''.2$.

Finally, Morganti et al. (1999) presented radio continuum maps for 29 Seyferts chosen from a total sample of 51 which satisfy $\delta < 0^\circ$ and $cz < 3600\text{ km s}^{-1}$, and which were considered by the authors to be “well classified.” The remaining 22 objects overlap heavily with studies such as those of Ulvestad & Wilson (1984b, 1989). VLA maps with resolution $\sim 1''$ were made at 6 cm for objects in the declination range $-30^\circ < \delta < 0^\circ$; the more southern objects were observed at 3.5 cm using the Australian Telescope Compact Array at a similar resolution.

Selection Biases in Seyfert Samples

The parent Seyfert samples on which many of the above radio surveys are based have inherent selection biases and completeness issues which need to be considered.

Because the Markarian survey selected objects by their ultraviolet excess, Seyfert galaxies derived from it are in principle biased toward members with unusually low dust extinction or exceptionally blue intrinsic spectra. Because Seyfert 2 nuclei display weaker featureless, blue continua than Seyfert 1 nuclei in their observed spectra (e.g., Koski 1978), any survey which selects objects by their ultraviolet or blue flux will have an overrepresentation of Seyfert 2 galaxies with intrinsically luminous, atypically blue nuclei, or, alternatively, Seyfert 2 galaxies with unusually high levels of ultraviolet emission arising exterior to the nucleus, such as in near-nuclear or circumnuclear star-forming regions. Ultraviolet selected Seyferts, therefore, contain mismatched populations of type 1 and type 2 objects. This selection bias may account for the frequent reports that Seyfert 2s tend to have a higher incidence of nuclear star formation compared to Seyfert 1s (e.g., Colina et al. 1997; González Delgado et al. 1998).

Spinoglio & Malkan (1989) argue that the *IRAS* 12 μm band minimizes wavelength-dependent selection effects for AGNs and that it carries an approximately constant fraction of the AGN bolometric luminosity. The “warm” *IRAS* samples selected at 25 and 60 μm have the advantage of being less susceptible to biases by Seyfert type (Keel et al. 1994; Kinney et al. 2000). Nonetheless, selection by mid-IR and far-IR emission most likely singles out unusually dusty objects, as well as those which may be simultaneously experiencing elevated levels of star formation, either in and near the nucleus or further out, since the large *IRAS* beam admits substantial contributions from the large-scale emission of the host galaxy. Kinney et al. (2000) note that the sample of Schmitt et al. (2001), for example, has a preponderance of highly inclined (edge-on) systems. And, as recognized by de Grijp et al. (1985, 1987) and Keel et al. (1988), while selection by far-IR colors identifies AGNs very effectively, it by no means produces complete samples. *IRAS*-based Seyfert samples are especially incomplete in low-luminosity objects because of severe confusion with the host galaxy.

Selection by hard X-rays in principle can yield relatively unbiased AGN samples. All known classes of AGNs emit X-rays, and photoelectric absorption is negligible at energies greater than 1 keV for gas columns $\lesssim 10^{25}\text{ atoms cm}^{-2}$. To date, however, the only all-sky hard X-ray survey is that by Piccinotti et al. (1982) based on the *HEAO-1* A-2 experiment. Because of the shallow limit of the survey [$f(2\text{--}10\text{ keV}) > 3 \times 10^{-11}\text{ erg s}^{-1}\text{ cm}^{-2}$], only a relatively limited number of intrinsically luminous sources are included.

An effective, albeit time-consuming, method to select AGNs is through optical spectroscopy of large numbers of galaxies chosen by well defined criteria, such as samples limited by optical magnitude. This category includes the CfA redshift survey (Huchra & Burg 1992) and the Palomar survey (Ho et al. 1995). AGNs are identified by diagnostic intensity ratios and widths of emission lines. This technique has two obvious limitations. First, heavily obscured sources could be missed in the optical, depending on the spatial scale and distribution of the dust. For example, dust tori on parsec or sub-parsec scale can easily hide the broad-line region and central continuum source, as is well known in some Seyfert nuclei. Nonetheless, this kind of obscuration in principle affects only the detailed classification of the AGN (as a “type 1” or “type 2” object); it would not cause the AGN to go unnoticed. The narrow-line regions of Seyferts typically extend over the inner few hundred parsecs or more, comparable to the physical scales sampled by ground-based optical spectrographs. The impact of dust distributed over galaxy-wide scales, such as in edge-on or interacting systems, is harder to gauge. In general, however, it appears that sensitive spectra can detect AGN emission lines even in highly obscured systems, presumably because the dust distribution is patchy. A significant fraction of ultraluminous IR galaxies, for instance, many of which are dusty and highly obscured, are recognized as AGNs (e.g., Veilleux, Kim, & Sanders 1999). Ho et al. (1997b) find that selection biases due to inclination effects do not appear to be severe in the Palomar survey. A second, potentially more serious complication arises from dilution of the AGN signal by emission from H II regions that might be included in the spectrograph aperture. Weaker AGNs can be outshined by brighter contaminating H II regions, especially in late-type galaxies undergoing vigorous star formation. This effect may account in part for the apparent dearth of AGNs among late-type galaxies in the Palomar survey (Ho et al. 1997b); it is unlikely to be significant in early-type (E–Sbc) galaxies, however, where the detection rate of AGNs is already very high ($\sim 60\%$; Ho et al. 1997b). To summarize: although AGN samples selected by optical spectroscopy are not immune from selection effects, they appear not to be very serious, especially

for early-type (E–Sbc) galaxies.

We close with a few comments regarding some of the existing optically selected Seyfert samples. The CfA Seyfert sample (Huchra & Burg 1992) is widely considered to be relatively free of systematic biases. We draw attention to some aspects of this sample which introduce subtle selection biases that appear to have been generally unrecognized. Huchra & Burg identified their Seyfert spectra by visual inspection of plots following the criteria stated in Huchra, Wyatt, & Davis (1982): objects whose permitted lines ($H\alpha$ and $H\beta$) have a full width near zero intensity (FWZI) larger than 2500 km s^{-1} are called Seyfert 1s, whereas those with $\text{FWZI}(H\alpha) = 600\text{--}2500 \text{ km s}^{-1}$ and a “large” $[\text{O III}] \lambda 5007/H\beta$ ratio are dubbed Seyfert 2s. They further define LINERs as objects with “strong” $[\text{O I}] \lambda 6300$ emission. Several criticisms can be raised against these selection criteria. First, the FWZI is a highly subjective parameter which depends sensitively on the S/N of a spectrum. The original CfA redshift survey, on which the Huchra & Burg catalog is based, was conducted largely with a photon-counting Reticon detector, a unique attribute of which is that the spectrum can be monitored in real time as photons accumulate. Since the primary objective was to obtain galaxy redshifts, the integration time was truncated once spectral features suitable for redshift determination could be discerned in the spectrum (Tonry & Davis 1979). The resulting nonuniform S/N of the data must make detection of broad, low-contrast wings on emission lines particularly difficult. Second, defining the FWZI for the narrow component of $H\alpha$, in the case of the Seyfert 2s, is especially treacherous, since in AGNs $H\alpha$ is quite heavily blended with the flanking $[\text{N II}] \lambda\lambda 6548, 6583$ lines, and the lines often have non-Gaussian, asymmetric profiles near the base (see Ho et al. 1997c for examples). Only those Seyfert 2s having the broadest, most extended wings observed with spectra of very high S/N would have made it into the final sample. Third, it is well known that the narrow lines of Seyferts span a substantial range of line widths, which are positively correlated with, among other things, the optical and radio luminosity of the nucleus (Phillips, Charles, & Baldwin 1983; Whittle 1985, 1992; Ho 1996). Selecting Seyferts based on an arbitrary lower threshold in narrow-line width, therefore, translates into selection by minimum optical and radio AGN power. Moreover, the lower bound of $\text{FWZI}(H\alpha) = 600 \text{ km s}^{-1}$ for Seyfert 2s chosen by Huchra et al. (1982) corresponds roughly to $\text{FWHM}(H\alpha) = 300 \text{ km s}^{-1}$, as judged from typical observed spectra. There are many Seyferts, of type 1 and type 2, whose narrow emission lines have widths smaller than this value. In the Palomar sample studied here, for example, the median FWHM for $[\text{N II}] \lambda 6583$, which serves as an acceptable surrogate for $H\alpha$ (see Ho et al. 1997a), is 275 km s^{-1} , with an interquartile range of 85 km s^{-1} . And finally, the CfA catalog considerably blurs the distinction between LINERs and Seyferts because of the somewhat subjective, nonstandard manner in which the classification criteria have been chosen.

We conclude, from the above discussion, that the CfA Seyfert sample is likely to be complete only for relatively bright objects with very conspicuous broad emission lines. In the case of Seyfert 2s, there is a preponderance of intrinsically luminous and more radio-powerful objects. A concrete comparison between the Palomar and CfA Seyfert samples may be illuminating. Of the 52 Seyferts in the Palomar sample, 39 formally fall within the limits of the CfA redshift survey, but only 12 (31%) — all classified as type 1 objects in the Palomar survey — were called Seyferts. Another nine objects which we classify as Seyferts were labeled LINERs. Even if we dispense with the arguably nebulous distinction between LINERs and Seyferts, the detection rate of the Palomar objects is still only 54% (21/39).

Lastly, we note that Seyfert samples drawn from heterogeneous literature sources are likely to contain complicated, ill defined incompleteness problems. This cautionary note would apply to studies which selected Seyferts based on spectral classifications “known” at the time. The samples in this category include those of Ulvestad & Wilson (1984b, 1989), Spinoglio & Malkan (1989), Rush et al. (1993), Nagar et al. (1999), and Morganti et al. (1999).

NOTES ON INDIVIDUAL OBJECTS

This Appendix provides a short description of each object, along with some remarks based on previously published radio observations. Note that the literature references are not meant to be comprehensive; we cite only the most pertinent information. The optical spectroscopic classification, taken from Ho et al. (1997a), is given in parentheses after the object name. See Section 2 for more details on the classification notation.

NGC 185 (S2). — Not detected. Heckman, Balick, & Crane (1980) also did not detect the galaxy at 6 cm ($S_6 < 1 \text{ mJy}$; $\Delta\theta = 1''.7$) or 20 cm ($S_{20} < 5 \text{ mJy}$; $\Delta\theta = 4''$). Although the weak emission lines in this object formally place it in the category of Seyferts, it is probable that this galaxy does not contain a genuine active nucleus. Instead, its emission lines may be powered by stellar processes. NGC 185 is one of the companions of M 31, and it is morphologically classified as a dwarf spheroidal galaxy, one with a diffuse center lacking a clear nucleus.

NGC 676 (S2:). — Not detected. No previous radio observations.

NGC 777 (S2/L2::). — The core appears to be slightly resolved at both frequencies along P.A. = 134° . There are no previous high-resolution radio observations.

NGC 1058 (S2). — Not detected. Cowan, Henry, & Branch (1988) obtained deep radio observations of the site of SN 1961V, but the nucleus of the galaxy, which lies within $1.3'$ of the supernova, was not detected at 6 cm ($S_6 < 0.09 \text{ mJy}$; $\Delta\theta = 0''.9$) or 20 cm ($S_{20} < 0.12 \text{ mJy}$; $\Delta\theta = 0''.9$).

NGC 1068, M 77 (S1.9). — This well known source has been extensively studied by many authors (e.g., Wilson & Ulvestad 1982b, 1983; Ulvestad, Neff, & Wilson 1987; Kukula et al. 1995; Gallimore, Baum, & O’Dea 1996). In addition to the prominent lobes associated with the AGN, our maps show traces of the $30''$ -diameter ($\sim 2 \text{ kpc}$) circumnuclear ring. Our measurement of the 6 cm core is in good agreement with the results of van der Hulst et al. (1981), whose data had a similar resolution as ours. Wilson & Ulvestad (1983) reported linearly-polarized 6 cm emission associated with the core and the northern lobe of NGC 1068. We detected these components ($S_{\text{pol},6}^I = 0.91 \text{ mJy}$ and 5.1 mJy , respectively), and,

in addition, we find significant polarization ($S_{\text{pol},6}^I = 5.3$ mJy) associated with the low-surface brightness feature to the northeast of the core (Fig. 16a). At 20 cm, the polarized signal near the core and in northern lobe can still be seen ($S_{\text{pol},20}^I = 1.2$ mJy and 1.1 mJy, respectively), although the northeastern feature appears much weaker.

NGC 1167 (S2). — The core appears clearly extended in our images. Our flux densities are in good agreement with those of Fanti et al. (1986), who quote $S_6 = 939$ mJy ($\Delta\theta = 0''.4$) and $S_{20} = 1780$ mJy ($\Delta\theta = 1''.4$). The higher resolution 6 cm data of Fanti et al. resolved the extended core into two components, which are also seen in the 2 cm map ($\Delta\theta = 0''.4$) of Bridle & Fomalont (1978). We detected linearly-polarized emission at 6 ($S_{\text{pol},6}^I = 1.8$ mJy) and 20 cm ($S_{\text{pol},20}^I = 2.1$ mJy). The polarization vectors, especially at 6 cm, appear to trace the slight extensions seen in the total-intensity image (Fig. 16b). The 20 cm polarization at the total-intensity peak is near the detection threshold of 0.2%, but we believe it to be real due to its continuity with the clearly extended polarized emission to the northeast.

NGC 1275 (S1.5). — The radio source 3C 84 associated with NGC 1275 possesses well known jets which have been documented on a variety of scales (Pedlar et al. 1990; Dhawan, Kellerman, & Romney 1998; Silver, Taylor, & Vermeulen 1998; Walker et al. 2000). The only measurable polarization was on the radio core, and well below the threshold of 0.2%, so there is no significant polarization detection for this galaxy.

NGC 1358 (S2). — Both Ulvestad & Wilson (1989) and Nagar et al. (1999) have noted that the core of NGC 1358 may be slightly extended. Our full-resolution 20 cm and tapered 6 cm maps show quite clearly that the nucleus is straddled by a jet-like linear feature with a total extent of ~ 8.6 kpc along P.A. = 101° . We note that the optical major axis of the galaxy is at P.A. = 165° , and so the extended radio emission is likely to be associated with the AGN rather than the galaxy disk.

NGC 1667 (S2). — Ulvestad & Wilson (1989) detected a core at 6 and 20 cm with flux densities comparable to ours, and Thean et al. (2000) give a similar value of $S_6 = 1.5$ mJy ($\Delta\theta = 0''.3$). Our tapered 6 cm map shows, in addition, a low surface brightness two-armed spiral feature, with a total linear extent of 14.5 kpc along P.A. $\approx 0^\circ$. The tapered 20 cm image only shows the central core and the high-surface brightness region of the southern spiral arm.

NGC 2273 (S2). — Our maps show the central source to be slightly extended in both bands, more so at 20 cm than at 6 cm. The 20 cm map of Ulvestad & Wilson (1984b), made with a resolution of $1''.4$, agrees well with ours. Their higher resolution 6 cm map ($\Delta\theta = 0''.4$), however, shows that the central source resolves into two components separated by $0''.9$ along the east-west direction. The $\Delta\theta \approx 4''$ 6 cm WSRT map of Baum et al. (1993) contains an extra resolved component not visible in our tapered 6 cm map.

NGC 2639 (S1.9). — We detect an unresolved core with an inverted spectrum ($\alpha_6^{20} = 0.47$). The higher resolution 6 cm map of Ulvestad & Wilson (1989) shows that the structure is suggestive of an incompletely-resolved triplet along P.A. $\approx 110^\circ$. This is consistent with other observations: 6 cm VLBA ($\Delta\theta = 2$ mas; Wilson et al. 1998), 6 cm VLA ($\Delta\theta = 0''.6$; Condon et al. 1982), and 3.6 cm VLA ($\Delta\theta = 0''.3$; Thean et al. 2000). Our 6 cm flux density (182 mJy) is significantly higher than that measured by the above-cited higher resolution studies (50–55 mJy). This can be interpreted as a resolution effect, although it can also result from source variability (Wilson et al. 1998). We further note that our maps show two additional “ears” of emission emerging on either side of the core along the north-south direction, roughly perpendicular to the major axis of the central component resolved by Ulvestad & Wilson (1989). Although these features are faint ($S_6 \approx 0.8$ and 0.7 mJy for the northern and southern component, respectively), they appear to be real because they are present in the full-resolution 6 and 20 cm maps, and the northern component barely peaks through in the tapered 6 cm map. Because of their uncertain relation to the AGN, however, we do not include these features in the radio morphological classification. Weak polarized emission is present at 6 cm ($S_{\text{pol},6}^I = 0.61$ mJy), but not at 20 cm ($S_{\text{pol},20}^P < 0.086$ mJy beam $^{-1}$). Most of the signal is associated with the core, but, quite interestingly, the north-south “ears” also appear to be polarized (Fig. 16e).

NGC 2655 (S2). — Keel & Hummel (1988) have reviewed the radio properties of NGC 2655. They noticed that apart from the central core, which had previously been studied by van der Hulst et al. (1981) and Hummel, van der Hulst, & Dickey (1984), there exists a jet-like feature located $\sim 15''$ (1.8 kpc) to the southeast. This patch of radio emission is evidently associated with an optical emission-line region, which could plausibly be powered by the radio plasma. Our data reveal an additional component, visible in the full-resolution and tapered 20 cm maps, on the *opposite* side of the nucleus. The new northwestern component, located approximately $40''$ (4.7 kpc) to the northwest at P.A. $\approx 110^\circ$, is weaker and more extended than the southeastern component. The flux densities from the tapered 20 cm map are $S_{20}(\text{SE}) = 8.0$ mJy and $S_{20}(\text{NW}) = 3.8$ mJy; the northwestern component is not detected at 6 cm. We believe that the northwestern component is real. Our tapered maps at both frequencies (see bottom right panel of Fig. 4c) also show a “tongue” of emission extending from the central core *toward* the northwestern component, strongly suggestive of an ejection origin for the latter. The nucleus was not detected in the VLBI experiment of Hummel et al. (1982). We detected weak linearly-polarized emission in our data. The signal is most readily seen in naturally-weighted maps tapered to $\Delta\theta = 2''.5$ (Fig. 16c). At 6 cm, the signal is roughly equally divided between the core ($S_{\text{pol},6}^I = 0.70$ mJy) and the southeastern feature ($S_{\text{pol},6}^I = 0.55$ mJy). The core polarization is less than 0.2% of the total-intensity peak, but it appears that there may be a significant signal in the polarization somewhat off the location of that peak. The emission at 20 cm is much less well defined; nevertheless, there do appear to be significant clumps of emission closely associated with the jet-like extensions in the total-intensity image. The individual clumps have peak flux densities $S_{\text{pol},20}^P \approx 0.25$ mJy beam $^{-1}$, approximately 10 times the rms in the map.

NGC 2685 (S2/T2:). — Not detected. Heckman et al. (1980) obtained less stringent upper limits at 6 cm ($S_6 < 2$ mJy;

$\Delta\theta = 1''.7$) and 20 cm ($S_{20} < 3$ mJy; $\Delta\theta = 4''$).

NGC 3031, M 81 (S1.5). — The nucleus of M 81 contains a bright (~ 90 mJy), variable, flat-spectrum radio core (e.g., Crane, Giuffrida, & Carlson 1976; de Bruyn et al. 1976; Bartel et al. 1982) with a one-sided jet on VLBI scales (Bietenholz, Bartel, & Rupen 2000). Its variability pattern is complex, with occasional outbursts during which the source doubles in brightness at higher frequencies (Ho et al. 1999b). The multi-configuration study by Kaufman et al. (1996) reveals a wealth of structural details. We reprocessed their 6 cm B-array and 20 cm A-array data, and most of the morphological features discussed by Kaufman et al. are recovered in our maps. The most spectacular feature is an arc-like structure located $45''$ to the northeast of the nucleus at P.A. $\approx 45^\circ$, highly suggestive of an outflow origin. There are, in addition, a number of compact sources located within the central $\sim 2''$ which are likely to be associated with M 81 (see Kaufman et al. 1996 for details). In deriving the largest linear extent of the source, we do not include the two compact sources labeled “57” and “75” in Figure 6 of Kaufman et al. (1996); their relation to the nucleus, though suggestive, is uncertain. Kaufman et al. (1996) have discussed extensively the polarization measurements of M 81. Here, we only remark that we have largely recovered the polarization structure found by Kaufman et al., the most notable feature being the high degree of polarization along the arc at 20 cm (Fig. 16d). At 6 cm, in addition to the weak polarized emission near the core reported by Kaufman et al., we also find some polarized signal associated with the arc; the polarization fraction approaches 100% in some locations along the arc. This very high value could be partly caused by resolving out much of the extended total-intensity emission, with the polarization changing on somewhat smaller scales to which the interferometers are more sensitive.

NGC 3079 (S2). — NGC 3079 belongs to a minority of edge-on spiral galaxies which exhibit anomalous extended emission along the minor axis. Apart from the strong nuclear source, the radio morphology is dominated by a striking system of loops and bubbles which strongly suggest an outflow origin (Duric & Seaquist 1988, and references therein). Our full-resolution images have resolved out most of the extended emission, although some of it is recovered in the tapered map. The extended, bubble-like component lies at P.A. $\approx 64^\circ$, close to the optical minor axis, which is at P.A. $= 75^\circ$. The nucleus, with a peak flux density of 90 mJy at 6 cm and 70 mJy at 20 cm in our $1''$ maps, has an angular size less than $0''.05$ at 15 GHz (Hummel et al. 1984; Carral, Turner, & Ho 1990), but it was not detected in the VLBI experiment of Hummel et al. (1982). Duric & Seaquist (1988) detected linearly-polarized 6 cm emission over the extent of the bubble-like feature and along the major axis of the galaxy’s disk. Our higher resolution map is shown in Figure 16g. The integrated polarized flux density of the bubble-like feature is $S_{\text{pol},6}^I = 12.4$ mJy, and the corresponding area-averaged polarization fraction is very high, $\sim 73\%$. This high percentage polarization may be caused by polarization structure on smaller scales than the total-intensity structure, as for NGC 3031. We did not detect polarization at 20 cm ($S_{\text{pol},20}^P < 0.096$ mJy beam $^{-1}$).

NGC 3147 (S2). — Several investigators have observed this galaxy at $\sim 1''$ resolution at 6 cm and find a compact, ~ 10 mJy core (Heckman et al. 1980; van der Hulst et al. 1981; Vila et al. 1990; Laurent-Muehleisen et al. 1997), consistent with our measurements. Vila et al. (1990) report $S_{20} = 10.6$ mJy, also in good agreement with our value. The 6 cm core shows weak, but significant, linear polarization (Fig. 16f); the peak signal, $S_{\text{pol},6}^P = 0.23$ mJy beam $^{-1}$, is approximately 10 times the rms. Polarization is not detected at 20 cm ($S_{\text{pol},20}^P < 0.11$ mJy beam $^{-1}$).

NGC 3185 (S2:). — Marginally detected at 6 cm but not at 20 cm. Hummel et al (1987) quote an uncertain detection of 0.7 mJy at 20 cm ($\Delta\theta = 1''.3$), considerably stronger than our upper limit of 0.16 mJy at a similar resolution.

NGC 3227 (S1.5). — The core of NGC 3227 is resolved at $\lesssim 1''$ resolution (Condon 1980; van der Hulst et al. 1981; Ulvestad et al. 1981; Ulvestad & Wilson 1984a; Hummel et al. 1987; Kukula et al. 1995), and at even higher resolution it breaks up into a $0''.4$ double source at P.A. $\approx 170^\circ$ (Mundell et al. 1995; $\Delta\theta = 0''.05$).

NGC 3254 (S2). — Not detected. Hummel et al. (1985) obtained a less stringent upper limit of $S_{20} < 1$ mJy ($\Delta\theta = 15''$).

NGC 3486 (S2). — Not detected. Hummel et al. (1987) obtained a less stringent upper limit of $S_{20} < 0.5$ mJy ($\Delta\theta = 1''.3$).

NGC 3516 (S1.2). — The shape of the synthesized beam is highly elongated, and our maps do not sample well the extended emission in this object. A strong (122 mJy at 6 cm, 326 mJy at 20 cm) background source $4''.3$ to the southeast also contributes sidelobe confusion. The central core component in NGC 3516 has been well documented in previous observations at 20, 6, 3.6, and 2 cm (Ulvestad & Wilson 1984b, 1989; Kukula et al. 1995; Nagar et al. 1999). The deeper 20 cm map ($\Delta\theta = 1''$) presented by Miyaji, Wilson, & Pérez-Fournon (1992) shows elongated, one-sided emission extending $20''$ northeast of the nucleus. The apparent spatial coincidence of the radio continuum with optical emission-line nebulae suggested to these authors that the two components are related to a bipolar gaseous outflow from the nucleus. Our 20 cm map clearly detected the same northeast extension, but we also see a weaker counterpart, of approximately the same length, toward the southwest. Both have roughly equal strength, each ~ 4 mJy. The double-sidedness of the linear feature is even more evident in the tapered 6 cm map. The total angular extent of the source is $\sim 51''$, which corresponds to a projected length of 9.6 kpc, along P.A. $= 38^\circ$. The southwestern extension can also be seen in the $\Delta\theta = 6''$ 6 cm WSRT image of Baum et al. (1993). It is of interest to note that the [O III] $\lambda 5007$ image of Miyaji et al. (1992) shows significant line emission to the southwest of the nucleus, roughly coincident with the southwestern jet component.

NGC 3735 (S2:). — The central core of NGC 3735 is embedded within a much larger disk of radio emission, which is best seen in the tapered 6 cm map. The extended component, with an angular diameter of $76''$ (15 kpc), has the same P.A. as that of the major axis of this edge-on galaxy, and is most likely associated with it. Irwin, English, & Sarathia (1999) show a low-resolution C-array 20 cm image of the galaxy. Although the fit of the central core in our maps formally indicates that it is slightly resolved, we consider this result to be unreliable because the derived major axis of the source lies along

the very elongated beam, and thus we classify the core as unresolved. Greenhill et al. (1997) reported the discovery of a nuclear water maser source in NGC 3735. They also observed the nucleus in the continuum at high resolution ($\Delta\theta \approx 0''.2\text{--}0''.4$). The nucleus was detected at 3.6 cm ($S_{3.6} = 0.6$ mJy) and 6 cm ($S_6 = 0.7$ mJy), but not at 2 cm ($S_2 < 1$ mJy). Their 6 cm flux density is consistent with our measurement ($S_6^P = 0.81$ mJy).

NGC 3941 (S2:). — Marginally detected at 6 cm but not at 20 cm. Wrobel & Heeschen (1991) placed an upper limit of 0.5 mJy in a 6 cm map made with $\Delta\theta = 5''$.

NGC 3976 (S2:). — A 0.5 mJy compact core was detected at 6 cm at the level of 11.5σ in the full-resolution map and 9σ in the tapered map. Yet, the 20 cm maps show no evidence of any significant signal, suggesting that the 6 cm source is absorbed at lower frequencies. There are no previously published radio observations of this galaxy.

NGC 3982 (S1.9). — Ulvestad & Wilson (1989) detected the source at 6 cm but not at 20 cm because of strong confusion; there is a 421 mJy background source in the field (cf. Table 4). Kukula et al. (1995) give a measurement at 3.6 cm. We detected an unresolved core at 6 and 20 cm. In addition, our tapered 6 cm map shows a weak, elongated feature roughly 4 kpc in length along P.A. = $0^\circ\text{--}10^\circ$. The feature is more evident toward the south of the nucleus, but it can be seen also extending to the north of it.

NGC 4051 (S1.2). — The radio structure of the nuclear region is known to be quite complex. At the highest available resolution, the central core splits into a small-scale double separated by $0''.4$ roughly in the east-west direction (Ulvestad & Wilson 1984b, 6 cm, $\Delta\theta = 0''.4$; Kukula et al. 1995, 3.6 cm, $\Delta\theta = 0''.3$). On a somewhat coarser resolution of $\sim 1''$, however, particularly at 20 cm, the source is dominated by emission extending toward the southwest (Ulvestad & Wilson 1984b; Vila et al. 1990). We detected this extended component in our maps, both at 6 and 20 cm, but we additionally see a fainter, oppositely-directed component to the northeast. The two-sidedness of the extended component is best viewed in our tapered 6 cm map; it can also be seen in the $\Delta\theta \approx 4''$ 6 cm WSRT map of Baum et al. (1993). The total linear extent of the “jet” is 1.2 kpc, and it lies along P.A. = 41° , perpendicular to the host-galaxy major axis (P.A. = 135°). We note, in passing, that the nucleus appears to be quite variable at 6 cm. The existing measurements made with $\Delta\theta \approx 1''$ show a spread of a factor of 6 in the 6 cm flux density (van der Hulst et al. 1981, 3.5 mJy; Ulvestad & Wilson 1984b, 6.0 mJy; Vila et al. 1990, 0.9 mJy; this paper, 3.2 mJy).

NGC 4138 (S1.9). — The nucleus is badly confused by two very strong sources ($S_{20} = 1.3$ and 0.33 Jy) located $\sim 3''.5$ to the southwest. The rms noise of the tapered 20 cm map is quite high. Nonetheless, a weak, compact core with an inverted spectrum ($S_6 = 0.78$ mJy, $S_{20} = 0.51$ mJy, $\alpha_6^{20} = 0.45$) is seen at the position of the optical nucleus. The only other previous radio observation is that of Wrobel & Heeschen (1991), who placed an upper limit of $S_6 < 2$ mJy ($\Delta\theta = 5''$).

NGC 4151 (S1.5). — The flux densities we measured are in good agreement with those of previous arcsecond-scale observations (e.g., Ulvestad et al. 1981, $S_6 = 125$ mJy), but our maps have insufficient resolution to reveal the intricate fine structure of this complex radio source. Sub-arcsecond VLA maps have been published by Carral et al. (1990; 2 cm), Kukula et al. (1995; 3.6 cm), and Pedlar et al. (1993; 3.6 and 6 cm), and a sub-arcsecond MERLIN image has been published by Booler, Pedlar, & Davies (1982; 18 cm). Ulvestad et al. (1998) presented VLBA 6 and 18 cm maps and an interpretation of the various radio components. Although this source has previously been extensively studied in the radio, we are not aware of any polarization measurements. We detected linearly-polarized emission both at 6 and 20 cm (Fig. 16h). The 6 cm emission appears slightly resolved ($S_{\text{pol},6}^I = 0.56$ mJy), with an extension to the west of the nucleus. At 20 cm the emission is concentrated in an unresolved clump ($S_{\text{pol},20}^P = 0.31$ mJy beam $^{-1}$) which is slightly displaced to the southwest of the nucleus.

NGC 4168 (S1.9:). — Our 6 cm flux density of 5.2 mJy for the compact source agrees well with the $\Delta\theta = 5''$ measurement of Wrobel & Heeschen (1991), who give $S_6 = 4.5$ mJy.

NGC 4169 (S2). — A very weak ($S_6^P = 0.19$ mJy, $S_{20}^P = 0.21$ mJy) source consistently appears slightly offset to the northwest of the optical position of the nucleus. This is seen also in the tapered 6 and 20 cm maps. Although the detection is somewhat marginal, it is probably real, especially since a 1.5 mJy source was detected in the lower resolution FIRST survey (Becker, White, & Helfand 1995; 20 cm, $\Delta\theta = 5''$). The position of the FIRST source agrees with our radio position.

NGC 4203 (L1.9). — The nucleus of this galaxy is classified as a LINER 1.9 and is not formally part of our Seyfert sample. Most of the radio flux is contained in a central, unresolved core, whose spectrum is inverted ($\alpha_6^{20} = 0.44$). Our 6 cm flux density of 11.2 mJy is in excellent agreement with those from previous studies (Fabbiano, Gioia, & Trinchieri 1989, $S_6 = 11.6$ mJy, $\Delta\theta \approx 1''$; Wrobel & Heeschen 1991, $S_6 = 12.5$ mJy, $\Delta\theta = 5''$), and our 20 cm measurement of 6.5 mJy matches well the value from the FIRST survey ($S_{20} = 6.9$ mJy). The inverted spectrum, accompanied by an apparent lack of variability, may indicate free-free absorption rather than synchrotron self-absorption.

NGC 4235 (S1.2). — The unresolved core has a flat or slightly inverted spectrum ($\alpha_6^{20} = 0.09$), consistent with previously reported flux densities from 2 to 20 cm (Ulvestad & Wilson 1984b, 1989; Kukula et al. 1995).

NGC 4258, M 106 (S1.9). — At the scale of our images, the nucleus of NGC 4258 appears as a slightly resolved 2–3 mJy core with a somewhat flat spectral index of $\alpha_6^{20} = -0.18$, in agreement with previous observations from 2 to 20 cm at similar resolution (Vila et al. 1990; Saikia et al. 1994; Turner & Ho 1994). Our 20 cm map shows low-surface brightness emission extending to the northwest and southeast. These belong to the complex set of “anomalous radio arms” best seen in the $\Delta\theta = 6''.5$ 20 cm VLA+WSRT image of van Albada & van der Hulst (1982). On VLBI scales, the central core breaks up into a sub-parsec jet oriented along the axis of the water maser disk (Herrnstein et al. 1997, 1998). The continuum source at 22 GHz varies by a factor of 2 on a timescale of weeks (Herrnstein et al. 1997).

NGC 4378 (S2). — This galaxy was marginally detected at 6 cm but not at 20 cm. There are no previously published radio observations.

NGC 4388 (S1.9). — Our maps show a strong central source which resolves into two peaks separated by $\sim 1''.9$ (150 pc) along P.A. $\approx 15^\circ$. Neither peak coincides with the position of the optical nucleus. A long ($\sim 15''$ or 1.2 kpc) plume of emission extends to the northeast, at the end of which it appears to bend abruptly. In the tapered 6 cm map we find an additional “tongue” of emission, $\sim 20''$ long, extending east of the central source. We fitted the central source with a two-Gaussian model. The northern peak (labeled “core-N” in Table 3) is brighter than the southern one (“core-S”) at 6 cm, but the situation is reversed at 20 cm. The spectral indices for the northern and southern peak are, respectively, $\alpha_6^{20} = -0.32$ and -0.80 . The overall morphology and flux densities derived from our maps agree very well with previous VLA studies conducted at similar resolutions (Stone, Wilson, & Ward 1988; Hummel & Saikia 1991). Higher resolution maps of NGC 4388 have been made at 2 cm (Carral et al. 1990), 3.6 cm (Kukula et al. 1995; Falcke, Wilson, & Simpson 1998; Mundell et al. 2000) and 6 cm (Mundell et al. 2000). These studies collectively show that the northern peak has a flat, or perhaps even slightly inverted, spectrum up to 2 cm, and that it is unresolved with a size upper limit of 70 mas. These characteristics suggest that the northern peak marks the true location of the nucleus, which is obscured at optical wavelengths.

NGC 4395 (S1.8). — NGC 4395 holds the distinction of hosting the Seyfert 1 nucleus with the lowest known optical luminosity (Filippenko & Sargent 1989), and one of the intrinsically weakest nuclear X-ray sources observed so far (Lira et al. 1999; Moran et al. 1999). NGC 4395 is also highly unusual as an AGN host because of its late Hubble type: it is classified as a Magellanic spiral (Sm), only 3.6 Mpc away, with an absolute magnitude of $M_{B_T}^0 = -17.2$. Sramek (1992; see also Moran et al. 1999) previously observed the nucleus with the VLA, and he detected an unresolved core with $S_6 = 0.6$ mJy ($\Delta\theta = 0''.4$) and $S_{20} = 1.24$ mJy ($\Delta\theta = 1''.4$). We measure $S_6 = 0.80$ mJy and $S_{20} = 1.68$ mJy, which indicates that the source has not varied significantly. Our 6 cm map is more sensitive than Sramek’s, who made use of archival data taken in 1982.

NGC 4450 (L1.9). — The nucleus of this galaxy is classified as a LINER 1.9 and is not formally part of our Seyfert sample. We detected a central, unresolved core, with a flat or mildly inverted spectrum ($\alpha_6^{20} = 0.07$). The previously reported measurement at 20 cm (Hummel et al. 1987; $S_{20} = 5.3$ mJy, $\Delta\theta = 1''.3$) agrees reasonably well with ours.

NGC 4472, M 49 (S2:). — Previous low-resolution maps find the radio core to be straddled by double-sided jets with an extent of $\sim 2'$ (Ekers & Kotanyi 1978; Condon & Broderick 1988). Our maps are insensitive to large-scale structure of this angular size, and we detect mainly an extended, elliptical source of length $\sim 11''$ (9 kpc) along P.A. $\approx 80^\circ$. Van der Hulst et al. (1981) and Fabbiano et al. (1989) have published 6 cm observations at similar resolution as ours. Birkinshaw & Davies (1985) quote an unpublished higher resolution map by R. Laing which shows that the central source resolves into a $3''$ jet along P.A. = 83° . We have detected linearly-polarized emission at 6 ($S_{\text{pol},6}^I = 1.26$ mJy) and 20 cm ($S_{\text{pol},20}^I = 0.40$ mJy). At both frequencies the strongest polarization lies offset from the peak in the total-intensity image (Fig. 16j); the polarization vectors appear to follow smaller scale structure which is not well resolved in our maps.

NGC 4477 (S2). — This galaxy was marginally detected at 6 cm but not at 20 cm. The very faint source ($S_6 = 0.18$ mJy in the untapered map and 0.26 mJy in the tapered map) is consistent with the published upper limit of $S_6 < 0.25$ mJy ($\Delta\theta \approx 8''$) by Fabbiano et al. (1989) and $S_6 < 0.5$ mJy ($\Delta\theta = 5''$) by Wrobel & Heeschen (1991).

NGC 4501, M 88 (S2). — We detected an unresolved core in both bands. Hummel et al. (1987) give a 20 cm flux density of $S_{20} = 2.7$ mJy ($\Delta\theta = 1''.3$), in reasonable agreement with our value. The galaxy was not detected at higher resolution ($\Delta\theta = 0''.3$) by Thean et al. (2000) at 3.6 cm; their upper limit of $S_{3.6} < 0.2$ mJy implies that the source is variable, it is somewhat resolved at the higher resolution, or its spectrum is much steeper than we inferred from our data ($\alpha_6^{20} = -0.48$).

NGC 4565 (S1.9). — VLA flux densities measured with $\sim 1''$ resolution have been published by van der Hulst et al. (1981) and Hummel et al. (1987), and a $\Delta\theta = 5''$ 20 cm detection is available from the FIRST survey. There is a spread of about a factor of 2 among the various measurements, including ours, suggesting that the nucleus may be variable.

NGC 4579, M 58 (S1.9/L1.9). — The previous $1''$ -resolution 6 cm map of van der Hulst et al. (1981) reported that the core of NGC 4579 is slightly extended along P.A. = 134° . Our maps, especially that at 20 cm (see also Hummel et al. 1987), show that the source is a double, separated by $4''.8$ along P.A. = 133° . We identify the brighter of the two with the nucleus, since it lies within $0''.6$ of the optical position of the nucleus, which is known to an accuracy of $\pm 0''.16$. Our data indicate that the core has an inverted spectrum ($\alpha_6^{20} = 0.49$), consistent with the measurements of Sadler et al. (1995) performed with the Parkes-Tidbinbilla Interferometer at 2.3 and 8.4 GHz ($\alpha = 0.19$). Other literature data include a VLBI detection at 6 cm ($S = 21$ mJy, quoted in Hummel et al. 1987), an Arecibo interferometer measurement at 2.4 GHz ($\Delta\theta = 1''$, $S = 20$ mJy; Turner, Helou, & Terzian 1988), and a VLA point at 3.6 cm ($\Delta\theta = 0''.3$, $S = 36.5$ mJy; Thean et al. 2000).

NGC 4639 (S1.0). — This galaxy was marginally detected at 6 cm but not at 20 cm. Hummel et al. (1985) obtained a less stringent upper limit of $S_{20} < 1$ mJy ($\Delta\theta = 15''$).

NGC 4698 (S2). — This galaxy was marginally detected at 6 cm but not at 20 cm. Hummel et al. (1987) obtained a less stringent upper limit of $S_{20} < 1.5$ mJy ($\Delta\theta = 1''.3$).

NGC 4725 (S2:). — Not detected. No previous high-resolution radio observations.

NGC 5033 (S1.5). — Previous 6 and 20 cm VLA data show an unresolved (Ulvestad & Wilson 1989; Collison et al. 1994; Kukula et al. 1995) or slightly resolved (van der Hulst et al. 1981) core. Kukula et al. remark that their C-array 3.6 cm map contains extended emission on a scale of $30''$. Our $1''$ maps show a slightly resolved, steep-spectrum ($\alpha_6^{20} = -0.52$)

core surrounded by a fluffy envelope with a major-axis diameter of $\sim 10''$ (0.9 kpc), roughly along the east-west direction. The extended emission is more prominent toward the east. The tapered maps further show a spectacular ridge of emission extended over $\sim 40''$ (3.6 kpc), running nearly north-south, along the galaxy major axis (P.A. = 170°). This large-scale feature lies roughly orthogonal to the $10''$ structure.

NGC 5194, M 51 (S2). — Ford et al. (1985) first drew attention to the morphological details of the radio emission in the center of this galaxy. In addition to the “extra-nuclear cloud” located $\sim 4''$ to the southeast of the nucleus, they noticed the ring-like appearance of the diffuse emission to the northwest of the nucleus. Ford et al. postulated that these features can plausibly be interpreted as bubbles created by a bipolar jet or outflow emanating from the nucleus. A much deeper, sub-arcsecond 6 cm map published by Crane & van der Hulst (1992) shows convincingly that the southeastern lobe of emission is connected to the nucleus by a thin, sinuous, jet-like feature, and the overall radio structure is embedded within the extended optical emission-line region imaged by Cecil (1988). Our maps qualitatively resemble the earlier versions. We wish only to draw attention to a knot of emission which lies $\sim 28''$ (1 kpc) to the northwest of the nucleus, roughly along a straight line connecting the other features. The source has $S_{20} = 1.9$ mJy and $S_6 = 1.4$ mJy, and it is unresolved. Since the density of background sources stronger than $S_{20} \approx 2$ mJy is $\sim 10^5$ sr $^{-1}$ (Windhorst et al. 1985), the probability that the source is unrelated to M 51 is quite small ($< 1\%$). It is unclear, however, whether the source is directly associated with the outflow itself, in which case the total extent of the radio source would be $35''$ (1.3 kpc) instead of $24''$ (0.9 kpc) as we have adopted in Table 5. Our flux densities for the nucleus are consistent with the values of Hummel et al. (1987; $S_{20} = 3.6$ mJy, $\Delta\theta = 1''.3$), Crane & van der Hulst (1992; $S_6 = 0.89$ mJy, $\Delta\theta = 0''.3$), and Turner & Ho (1994; $S_6 = 1.1$ mJy, $\Delta\theta = 1''.1$). Thean et al. (2000) give $S_{3.6} = 0.5$ mJy ($\Delta\theta = 0''.3$). Crane & van der Hulst (1992) remarked that their 6 cm data show marginally significant linearly-polarized emission coincident with the extra-nuclear cloud to the southeast. Our maps confirm this finding, both at 6 and 20 cm (Fig. 16i); in addition, a number of other peaks ($S_{\text{pol},6}^P \approx S_{\text{pol},20}^P \approx 0.2$ mJy beam $^{-1}$) of comparable statistical significance appear to be associated with ring-like feature to the northwest of the nucleus.

NGC 5273 (S1.5). — We detect a compact, unresolved core at both frequencies. The source is slightly resolved along P.A. = 0° in the 6 cm data of Ulvestad & Wilson (1984b). Both Kukula et al. (1995) and Nagar et al. (1999) have observed NGC 5273 at 3.6 cm with $\Delta\theta = 0''.3$; the former did not detect the nucleus ($S_{3.6} < 0.23$ mJy), but the latter did ($S_{3.6} = 0.6$ mJy), which suggests that the source is variable.

NGC 5395 (S2/L2). — Not detected. Hummel et al. (1987) obtained a less stringent upper limit of $S_{20} < 0.4$ mJy ($\Delta\theta = 1''.3$).

NGC 5548 (S1.5). — The classic triple linear structure of NGC 5548, consisting of a compact core and oppositely-directed lobes, is well known (Wilson & Ulvestad 1982a; Kukula et al. 1995; Nagar et al. 1999; Wrobel 2000). Our maps are consistent with those of previous studies. The core is unresolved at our resolution, and the total extent of the jets is $\sim 15''$ (5 kpc) along P.A. = 163° . We find evidence for weak ($S_{\text{pol},6}^P \approx S_{\text{pol},20}^P \approx 0.2$ mJy beam $^{-1}$) linearly-polarized emission associated with the extended emission (Fig. 16k).

NGC 5631 (S2/L2). — Although this source is quite weak, we believe it to be real because it was detected in both bands at full-resolution and in the tapered 6 cm map. The only previous radio observation is that of Wrobel & Heeschen (1991), who obtained an upper limit of $S_6 < 0.5$ mJy with $\Delta\theta = 5''$. Our measurements are consistent with this upper limit.

NGC 6951 (S2). — NGC 6951 harbors a Seyfert 2 nucleus which is surrounded by a 1 kpc-diameter circumnuclear starburst ring (Barth et al. 1995). Our full-resolution maps depict the ring with much greater clarity than in previous radio maps made with similar resolution (Vila et al. 1990; Saikia et al. 1994). The nucleus, which contains only $\sim 10\%$ of the total flux in either band, has a steep spectrum ($\alpha_6^{20} = -0.90$). Although it appears to be slightly resolved in one direction, the apparent elongation is along the direction of the beam, and we consider the source to be unresolved.

NGC 7479 (S1.9). — Condon, Frayer, & Broderick (1991) and Hummel et al. (1987) have previously detected a slightly resolved ~ 6 mJy core at 20 cm based on $\Delta\theta = 1''.5$ maps. We find the core to be unresolved at our resolution, and our full-resolution 20 cm and tapered 6 and 20 cm maps show an additional curved extension to the north, and perhaps a weaker, but shorter, component to the south. The total extent of the linear feature is $36''$, or 5.7 kpc. We find evidence for weak ($S_{\text{pol},6}^P \approx S_{\text{pol},20}^P \approx 0.1$ – 0.2 mJy beam $^{-1}$) linearly-polarized emission associated with the extended emission (Fig. 16l).

NGC 7743 (S2). — This galaxy has been observed with the C-array at 6 cm by Wrobel & Heeschen (1991) and with the A-array at 3.6 and 20 cm by Nagar et al. (1999). We reprocessed the archival 6 and 20 cm data, and the flux densities of the compact source measured from our maps are in good agreement with the published values. In order to estimate the spectral index, we tapered the 20 cm A-array map to a resolution comparable to that of the full-resolution 6 cm C-array map ($\Delta\theta \approx 3''.8$); we measure $\alpha_6^{20} = -0.49$.

REFERENCES

- | | |
|--|---|
| <p>Argyle, R. W., & Eldridge, P. 1990, MNRAS, 243, 504
 Bartel, N., et al. 1982, ApJ, 262, 556
 Barth, A. J., Ho, L. C., Filippenko, A. V., & Sargent, W. L. W. 1995, AJ, 110, 1009
 Barth, A. J., Reichert, G. A., Filippenko, A. V., Ho, L. C., Shields, J. C., Mushotzky, R. F., & Puchanewicz, E. M. 1996, AJ, 112, 1829</p> | <p>Baum, S. A., O’Dea, C. P., Dallacassa, D., de Bruyn, A. G., & Pedlar, A. 1993, ApJ, 419, 553
 Becker, R. H., White, R. L., & Helfand, D. J. 1995, ApJ, 450, 559
 Bicknell, G. V., Dopita, M. A., Tsvetanov, Z., & Sutherland, R. S. 1998, ApJ, 495, 680
 Bietenholz, M. F., Bartel, N., & Rupen, M. P. 2000, ApJ, 532, 895
 Birkinshaw, M., & Davies, R. L. 1985, ApJ, 291, 32
 Booler, R. V., Pedlar, A., & Davies, R. D. 1982, MNRAS, 199, 229</p> |
|--|---|

- Bridle, A. H., & Fomalont, E. B. 1978, *MNRAS*, 185, 67P
- Bridle, A. H., & Schwab, F. R. 1999, *Synthesis Imaging in Radio Astronomy II*, ed. G. B. Taylor, C. L. Carilli, & R. A. Perley (San Francisco: ASP), 371
- Browne, I. W. A., Patnaik, A. R., Wilkinson, P. N., & Wrobel, J. W. 1998, *MNRAS*, 293, 257
- Carral, P., Turner, J. L., & Ho, P. T. P. 1990, *ApJ*, 362, 434
- Cecil, G. 1988, *ApJ*, 329, 38
- Clark, B. G. 1980, *A&A*, 89, 377
- Clements, E. D. 1981, *MNRAS*, 197, 829
- . 1983, *MNRAS*, 204, 811
- Cohen, R. D. 1983, *ApJ*, 273, 489
- Colina, L., García Vargas, M. L., Goltzalez Delgado, R. M., Mas-Hesse, J. M., Pérez, E., Alberdi, A., & Krabbe, A. 1997, *ApJ*, 488, L71
- Collison, P. M., Saikia, D. J., Pedlar, A., Axon, D. J., & Unger, S. W. 1994, *MNRAS*, 268, 203
- Condon, J. J. 1980, *ApJ*, 242, 894
- . 1997, *PASP*, 109, 166
- Condon, J. J., & Broderick, J. J. 1988, *AJ*, 96, 30
- Condon, J. J., Condon, M. A., Gisler, G., & Puschell, J. J. 1982, *ApJ*, 252, 102
- Condon, J. J., Frayer, D. T., & Broderick, J. J. 1991, *AJ*, 101, 362
- Cornwell, T. J., & Fomalont, E. B. 1999, *Synthesis Imaging in Radio Astronomy II*, ed. G. B. Taylor, C. L. Carilli, & R. A. Perley (San Francisco: ASP), 187
- Cotton, W. D., Condon, J. J., & Arbizzani, E. 1999, *ApJS*, 125, 409
- Cowan, J. J., Henry, R. B. C., & Branch, D. 1988, *ApJ*, 329, 116
- Crane, P. C., Giuffrida, B., & Carlson, J. B. 1976, *ApJ*, 203, L113
- Crane, P. C., & van der Hulst, J. M. 1992, *AJ*, 103, 1146
- Dahari, O., & De Robertis, M. M. 1988, *ApJS*, 67, 249
- de Bruyn, A. G., Crane, P. C., Price, R. M., & Carlson, J. 1976, *A&A*, 46, 243
- de Bruyn, A. G., & Wilson, A. S. 1976, *A&A*, 53, 93
- . 1978, *A&A*, 64, 433
- de Grijp, M. H. K., Keel, W. C., Miley, G. K., Goudfrooij, P., & Lub, J. 1992, *A&AS*, 96, 389
- de Grijp, M. H. K., Miley, G. K., & Lub, J. 1987, *A&AS*, 70, 95
- de Grijp, M. H. K., Miley, G. K., Lub, J., & de Jong, T. 1985, *Nature*, 314, 240
- de Vaucouleurs, G., de Vaucouleurs, A., Corwin, H. G., Jr., Buta, R. J., Paturel, G., & Fouqué, R. 1991, *Third Reference Catalogue of Bright Galaxies* (New York: Springer)
- Dhawan, V., Kellermann, K. I., & Romney, J. D. 1998, *ApJ*, 498, L111
- Duric, N., & Seaquist, E. R. 1988, *ApJ*, 326, 574
- Edelson, R. 1987, *ApJ*, 313, 651
- Ekers, R. D., & Kotanyi, C. G. 1978, *A&A*, 67, 47
- Eubanks, T. M., et al. 1998, *USNO - Ref Frame 1998-6*, unpublished
- Fabbiano, G., Gioia, I. M., & Trinchieri, G. 1989, *ApJ*, 347, 127
- Falcke, H., Wilson, A. S., & Simpson, C. 1998, *ApJ*, 502, 199
- Fanaroff, B. L., & Riley, J. M. 1974, *MNRAS*, 167, 31P
- Fanti, C., Fanti, R., de Ruiter, H. R., & Parma, P. 1986, *A&AS*, 65, 145
- Feigelson, E. D., & Nelson, P. I. 1985, *ApJ*, 293, 192
- Filippenko, A. V., Ho, L. C., & Sargent, W. L. W. 1993, *ApJ*, 410, L75
- Filippenko, A. V., & Sargent, W. L. W. 1989, *ApJ*, 342, L11
- Ford, H. C., Crane, P. C., Jacoby, G. H., Lawrie, D. G., & van der Hulst, J. M. 1985, *ApJ*, 293, 132
- Gallimore, J. F., Baum, S., & O'Dea, C. P. 1996, *ApJ*, 458, 136
- Giuricin, G., Mardrossian, F., & Mezzetti, M. 1988, *A&A*, 203, 39
- Giuricin, G., Mardrossian, F., Mezzetti, M., & Bertotti, G. 1990, *ApJS*, 72, 551
- González Delgado, R. M., Heckman, T., Leitherer, C., Meurer, G., Krolik, J. H., Wilson, A. S., Kinney, A. L., & Koratkar, A. P. 1998, *ApJ*, 505, 174
- Goodrich, R. W. 1989, *ApJ*, 342, 224
- Greenhill, L. J., Herrnstein, J. R., Moran, J. M., Menten, K. M., & Velusamy, T. 1997, *ApJ*, 486, L15
- Heckman, T. M., Balick, B., & Crane, P. C. 1980, *A&AS*, 40, 295
- Heckman, T. M., van Breugel, W. J. M., Miley, G. K., & Butcher, H. R. 1983, *AJ*, 88, 1077
- Herrnstein, J., Greenhill, L. J., Moran, J. M., Diamond, P., Inoue, M., Nakai, N., & Miyoshi, M. 1998, *ApJ*, 497, L69
- Herrnstein, J., Moran, J. M., Greenhill, L. J., Diamond, P., Miyoshi, M., Nakai, N., & Inoue, M. 1997, *ApJ*, 475, L17
- Ho, L. C. 1996, in *The Physics of LINERs in View of Recent Observations*, ed. M. Eracleous et al. (San Francisco: ASP), 103
- Ho, L. C., Filippenko, A. V., & Sargent, W. L. W. 1995, *ApJS*, 98, 477
- . 1996, *ApJ*, 462, 183
- . 1997a, *ApJS*, 112, 315
- . 1997b, *ApJ*, 487, 568
- Ho, L. C., Filippenko, A. V., Sargent, W. L. W., & Peng, C. Y. 1997c, *ApJS*, 112, 391
- Ho, L. C., Ptak, A., Terashima, Y., Kunieda, H., Serlemitsos, P. J., Yaqoob, T., & Koratkar, A. P. 1999a, *ApJ*, 525, 168
- Ho, L. C., Van Dyk, S. D., Pooley, G. G., Sramek, R. A., & Weiler, K. W. 1999b, *AJ*, 118, 843
- Högbom, J. A. 1974, *A&AS*, 15, 417
- Huchra, J. P., & Burg, R. 1992, *ApJ*, 393, 90
- Huchra, J. P., Wyatt, W. F., & Davis, M. 1982, *AJ*, 87, 1628
- Hummel, E., Fanti, C., Parma, P., & Schilizzi, R. T. 1982, *A&A*, 114, 400
- Hummel, E., Pedlar, A., van der Hulst, J. M., & Davies, R. D. 1985, *A&AS*, 60, 293
- Hummel, E., & Saikia, D. J. 1991, *A&A*, 249, 43
- Hummel, E., van der Hulst, J. M., & Dickey, J. M. 1984, *A&A*, 134, 207
- Hummel, E., van der Hulst, J. M., Keel, W. C., & Kennicutt, R. C., Jr. 1987, *A&AS*, 70, 517
- Irwin, J. A., English, J., & Sorathia, B. 1999, *AJ*, 117, 2102
- Kailey, W. F., & Lebofsky, M. J. 1988, *ApJ*, 326, 653
- Kaufman, M., Bash, F. N., Crane, P. C., & Jacoby, G. H. 1996, *AJ*, 112, 1021
- Keel, W. C. 1984, *ApJ*, 282, 75
- Keel, W. C., de Grijp, M. H. K., & Miley, G. K. 1988, *A&A*, 203, 250
- Keel, W. C., de Grijp, M. H. K., Miley, G. K., & Zheng, W. 1994, *A&A*, 283, 791
- Keel, W. C., & Hummel, E. 1988, *A&A*, 194, 90
- Kinney, A. L., Schmitt, H. R., Clarke, C. J., Pringle, J. E., Ulvestad, J. S., & Antonucci, R. R. J. 2000, *ApJ*, 537, 152
- Koski, A. T. 1978, *ApJ*, 223, 56
- Kukula, M. J., Pedlar, A., Baum, S. A., O'Dea, C. P. 1995, *MNRAS*, 276, 1262
- Laurent-Muehleisen, S. A., Kollgaard, R. I., Ryan, P. J., Feigelson, E. D., Brinkmann, W., & Siebert, J. 1997, *A&AS*, 122, 235
- Lira, P., Lawrence, A., O'Brien, P., Johnson, R. A., Terlevich, R., & Bannister, N. 1999, *MNRAS*, 304, 109
- Low, F. J., Huchra, J. P., Kleinmann, S. G., & Cutri, R. M. 1988, *ApJ*, 327, L41
- Ma, C., Arias, E. F., Eubanks, T. M., Fey, A. L., Gontier, A.-M., Jacobs, C. S., Sovers, O. J., Archinal, B. A., & Charlot, P. 1998, *AJ*, 116, 516
- Maiolino, R., & Rieke, G. H. 1995, *ApJ*, 454, 95
- Meurs, E. J. A., & Wilson, A. S. 1981, *A&AS*, 45, 99
- . 1984, *A&A*, 136, 206
- Miyaji, T., Wilson, A. S., & Pérez-Fournon, I. 1992, *ApJ*, 385, 137
- Moran, E. C., Filippenko, A. V., Ho, L. C., Shields, J. C., Belloni, T., Comastri, A., Snowden, S. L., & Sramek, R. A. 1999, *PASP*, 111, 801
- Morganti, R., Tsvetanov, Z. I., Gallimore, J., & Allen, M. G. 1999, *A&AS*, 137, 457
- Mundell, C. G., Holloway, A. J., Pedlar, A., Meaburn, J., Kukula, M. J., & Axon, D. J. 1995, *MNRAS*, 275, 67
- Mundell, C. G., Wilson, A. S., Ulvestad, J. S., & Roy, A. L. 2000, *ApJ*, 529, 816
- Nagar, N. M., Wilson, A. S., Mulchaey, J. S., & Gallimore, J. F. 1999, *ApJS*, 120, 209
- Norris, R. P., Allen, D. A., Sramek, R. A., Kesteven, M. J., & Troup, E. R. 1990, *ApJ*, 359, 291
- Norris, R. P., Kesteven, M. J., Allen, D. A., & Troup, E. R. 1988, *MNRAS*, 234, 51P
- Osterbrock, D. E. 1981, *ApJ*, 249, 462
- Osterbrock, D. E., & De Robertis, M. M. 1985, *PASP*, 97, 1129
- Osterbrock, D. E., & Pogge, R. W. 1985, *ApJ*, 297, 166
- Patnaik, A. R., Browne, I. W. A., Wilkinson, P. N., & Wrobel, J. M. 1992, *MNRAS*, 254, 665
- Pedlar, A., Ghataure, H. S., Davies, R. D., Harrison, B. A., Perley, R., Crane, P. C., & Unger, S. W. 1990, *MNRAS*, 246, 477
- Pedlar, A., Kukula, M. J., Longley, D. P. T., Muxlow, T. W. B., Axon, D. J., Baum, S., O'Dea, C., & Unger, S. W. 1993, *MNRAS*, 263, 471
- Phillips, M. M., Charles, P. A., & Baldwin, J. A. 1983, *ApJ*, 266, 485
- Piccinotti, G., Mushotzky, R. F., Boldt, E. A., Holt, S. S., Marshall, F. E., Serlemitsos, P. J., & Shafer, R. A. 1982, *ApJ*, 253, 485
- Roy, A. L., Norris, R. P., Kesteven, M. J., Troup, E. R., & Reynolds, J. E. 1994, *ApJ*, 432, 496
- Rush, B., Malkan, M. A., & Edelson, R. A. 1996, *ApJ*, 473, 130
- Rush, B., Malkan, M. A., & Spinoglio, L. 1993, *ApJS*, 89, 1
- Sadler, E. M., Jenkins, C. R., & Kotanyi, C. G. 1989, *MNRAS*, 240, 591
- Sadler, E. M., Slee, O. B., Reynolds, J. E., & Roy, A. L. 1995, *MNRAS*, 276, 1373
- Saikia, D. J., Pedlar, A., Unger, S. W., & Axon, D. J. 1994, *MNRAS*, 270, 46
- Sandage, A. R., & Tammann, G. A. 1981, *A Revised Shapley-Ames Catalog of Bright Galaxies* (Washington, DC: Carnegie Inst. of Washington)

- Sandage, A. R., Tammann, G. A., & Yahil, A. 1979, *ApJ*, 232, 352
- Schmitt, H. R., Ulvestad, J. S., Antonucci, R. R. J., & Kinney, A. L. 2001, *ApJ*, in press
- Silver, C. S., Taylor, G. B., & Vermeulen, R. C. 1998, *ApJ*, 502, 229
- Slee, O. B., Sadler, E. M., Reynolds, J. E., & Ekers, R. D. 1994, *MNRAS*, 269, 928
- Spinoglio, L., & Malkan, M. A. 1989, *ApJ*, 342, 83
- Sramek, R. 1992, in *Relationships between AGNs and Starburst Galaxies*, ed. A. V. Filippenko (San Francisco: ASP), 273
- Stone, J. L., Jr., Wilson, A. S., & Ward, M. J. 1988, *ApJ*, 330, 105
- Thean, A., Pedlar, A., Kukula, M. J., Baum, S. A., & O'Dea, C. P. 2000, *MNRAS*, 314, 573
- Thompson, A. R., Clark, B. G., Wade, C. M., & Napier, P. J. 1980, *ApJS*, 44, 151
- Tonry, J., & Davis, M. 1979, *AJ*, 84, 1511
- Tully, R. B. 1988, *Nearby Galaxies Catalog* (Cambridge: Cambridge Univ. Press)
- Turner, J. L., & Ho, P. T. P. 1994, *ApJ*, 421, 122
- Turner, K. C., Helou, G., & Terzian, Y. 1988, *PASP*, 100, 452
- Ulvestad, J. S. 1986, *ApJ*, 310, 136
- Ulvestad, J. S., Antonucci, R. R. J., & Goodrich, R. W. 1995, *AJ*, 109, 81
- Ulvestad, J. S., & Ho, L. C. 2001, in preparation
- Ulvestad, J. S., Neff, S. G., & Wilson, A. S. 1987, *AJ*, 93, 22
- Ulvestad, J. S., Roy, A. L., Colbert, E. J. M., & Wilson, A. S. 1998, *ApJ*, 496, 196
- Ulvestad, J. S., & Wilson, A. S. 1984a, *ApJ*, 278, 544
- . 1984b, *ApJ*, 285, 439
- . 1989, *ApJ*, 343, 659
- Ulvestad, J. S., Wilson, A. S., & Sramek, R. A. 1981, *ApJ*, 247, 419
- Unger, S. W., Lawrence, A., Wilson, A. S., Elvis, M., & Wright, A. E. 1987, *MNRAS*, 228, 521
- van Albada, T. S., & van der Hulst, J. M. 1982, *A&A*, 115, 263
- van der Hulst, J. M., Crane P. C., & Keel, W. C. 1981, *AJ*, 86, 1175 (Erratum: 1983, *AJ*, 88, 138)
- van Moorsel, G., Kembell, A., & Greisen, E. 1996, in *Astronomical Data Analysis Software and Systems V*, ed. G. H. Jacoby & J. Barnes (San Francisco: ASP), 37
- Veilleux, S., Kim, D.-C., & Sanders, D. B. 1999, *ApJ*, 522, 113
- Véron, P. 1979, *A&A*, 78, 46
- Vila, M. B., Pedlar, A., Davies, R. D., Hummel, E., & Axon, D. J. 1990, *MNRAS*, 242, 379
- Walker, R. C., Dhawan, V., Romney, J. D., Kellerman, K. I., & Vermeulen, R. C. 2000, *ApJ*, 530, 233
- Wardle, J. F. C., & Kronberg, P. P. 1974, *ApJ*, 194, 249
- Weiler, K. W., Sramek, R. A., Panagia, N., van der Hulst, J. M., & Salvati, M. 1986, *ApJ*, 301, 790
- Whittle, M. 1985, *MNRAS*, 213, 33
- . 1992, *ApJS*, 79, 49
- Wilkinson, P. N., Browne, I. W. A., Patnaik, A. R., Wrobel, J. M., & Sorathia, B. 1998, *MNRAS*, 300, 790
- Wilson, A. S. 1997, in *IAU Colloq. 159, Emission Lines in Active Galaxies: New Methods and Techniques*, ed. B. M. Peterson, F.-Z. Cheng, & A. S. Wilson (San Francisco: ASP), 264
- Wilson, A. S., et al. 1998, *ApJ*, 505, 587
- Wilson, A. S., & Meurs, E. J. A. 1982, *A&AS*, 50, 217
- Wilson, A. S., & Ulvestad, J. S. 1982a, *ApJ*, 260, 56
- . 1982b, *ApJ*, 263, 576
- . 1983, *ApJ*, 275, 8
- Wilson, A. S., & Willis, A. J. 1980, *ApJ*, 240, 429
- Windhorst, R. A., Miley, G. K., Owen, F. N., Kron, R. G., & Koo, D. C. 1985, *ApJ*, 289, 494
- Wrobel, J. M. 2000, *ApJ*, 531, 716
- Wrobel, J. M., & Heeschen, D. S. 1991, *AJ*, 101, 148

FIGURE CAPTIONS

Fig. 1. — Number distributions of (a) distance, (b) total absolute blue magnitude (corrected for internal extinction), (c) morphological type index, T (-3 to $-1 = S0$, $1 = Sa$, $3 = Sb$, $5 = Sc$, $7 = Sd$, $9 = Sm$), and (d) extinction-corrected luminosity of the narrow $H\alpha$ emission line for the Palomar Seyfert sample. The morphologically peculiar galaxy NGC 1275 was omitted from (c). The type 1 objects are shown as shaded histograms, and the total sample (types 1 and 2) is denoted by the unshaded histograms. All the data are taken from Ho et al. (1997a) and are given in Tables 1 and 5.

Fig. 2. — Full-resolution ($\Delta\theta \approx 1''$), uniformly-weighted maps at 20 cm (a) and 6 cm (b), and tapered, naturally-weighted maps at 6 cm (c) for NGC 185, NGC 676, NGC 777, and NGC 1058. The resolution of the tapered maps, given in Table 3, is either $\Delta\theta \approx 2''.5$ or $3''.6$. Contour plots have been overlaid on the greyscale images to improve the visibility of the full dynamic range of the maps. Panels (a) and (b) are registered, and they have the same dimensions ($30'' \times 30''$). The dimensions of panel (c) have been optimized for each galaxy. The restoring beam is depicted as a hatched ellipse on the lower left-hand corner of each map. The maps display contour levels of $\text{rms} \times (-6, -3, 3, 6, 12, 24, 48, \dots)$; the rms values for the maps are listed in Table 3. The optical position of the galaxy is marked with a cross, the semi-major length of which corresponds to the 1σ uncertainties given in Table 1.

Fig. 3. — Maps for NGC 1068, NGC 1167, NGC 1275, and NGC 1358. Same as in Fig. 2.

Fig. 4. — Maps for NGC 1667, NGC 2273, NGC 2639, and NGC 2655. Same as in Fig. 2. A tapered 20 cm map of NGC 2655 is also shown as the top image in panel (c).

Fig. 5. — Maps for NGC 2685, NGC 3031, NGC 3079, and NGC 3147. Same as in Fig. 2, except that the dimensions of panels (a) and (b) for NGC 3079 are $48'' \times 48''$.

Fig. 6. — Maps for NGC 3185, NGC 3227, NGC 3254, and NGC 3486. Same as in Fig. 2.

Fig. 7. — Maps for NGC 3516, NGC 3735, NGC 3941, and NGC 3976. Same as in Fig. 2.

Fig. 8. — Maps for NGC 3982, NGC 4051, NGC 4138, and NGC 4151. Same as in Fig. 2.

Fig. 9. — Maps for NGC 4168, NGC 4169, NGC 4203, and NGC 4235. Same as in Fig. 2.

Fig. 10. — Maps for NGC 4258, NGC 4378, NGC 4388, and NGC 4395. Same as in Fig. 2.

Fig. 11. — Maps for NGC 4450, NGC 4472, NGC 4477, and NGC 4501. Same as in Fig. 2.

Fig. 12. — Maps for NGC 4565, NGC 4579, NGC 4639, and NGC 4698. Same as in Fig. 2.

Fig. 13. — Maps for NGC 4725, NGC 5033, NGC 5194, and NGC 5273. Same as in Fig. 2, except that the dimensions of panels (a) and (b) for NGC 5194 are $40'' \times 40''$.

Fig. 14. — Maps for NGC 5395, NGC 5548, NGC 5631, and NGC 6951. Same as in Fig. 2.

Fig. 15. — Maps for NGC 7479 and NGC 7743. Same as in Fig. 2. The 6 cm images of NGC 7743 were made with the C-configuration rather than the B-configuration, and thus have poorer resolution than the other images.

Fig. 16. — Objects with detected linear polarization. The contours show maps of total intensity, as in Fig. 2. The maps are uniformly weighted and have full resolution ($\Delta\theta \approx 1''$). The vectors represent linearly-polarized emission derived from naturally-weighted maps with $\Delta\theta \approx 1''.4$; the position angles of the vectors denote the direction of the electric field. Only signal in excess of 3 times the rms is shown. For NGC 2655, NGC 3031, and NGC 7479, both the total-intensity and linearly-polarized maps are naturally weighted and tapered to $\Delta\theta \approx 2''.5$. A polarization vector $1''$ long represents the following linearly-polarized flux density: (a) 1 mJy beam^{-1} , NGC 1068; (b) 1 mJy beam^{-1} , NGC 1167; (c) $0.1 \text{ mJy beam}^{-1}$, NGC 2655; (d) $0.1 \text{ mJy beam}^{-1}$, NGC 3031; (e) $0.5 \text{ mJy beam}^{-1}$, NGC 2639; (f) $0.5 \text{ mJy beam}^{-1}$, NGC 3147; (g) $0.25 \text{ mJy beam}^{-1}$, NGC 3079; (h) $0.25 \text{ mJy beam}^{-1}$, NGC 4151; (i) $0.25 \text{ mJy beam}^{-1}$, NGC 5194; (j) $0.5 \text{ mJy beam}^{-1}$, NGC 4472; (k) $0.25 \text{ mJy beam}^{-1}$, NGC 5548; and (l) $0.1 \text{ mJy beam}^{-1}$, NGC 7479.

Fig. 17. — Number distributions of radio powers. The panels show, from top to bottom, measurements for the total integrated power at 6 cm, the peak core power at 6 cm, the total integrated power at 20 cm, and the peak core power at 20 cm. The shaded regions of the histogram denote upper limits.

Fig. 18. — Number distributions of (a) linear source size and (b) spectral index between 6 and 20 cm. The shaded regions of the histogram denote upper limits.

TABLE 1: THE GALAXY SAMPLE

Galaxy	AGN Class	Hubble Type	T Index	B_T (mag)	D (Mpc)	$\alpha(J2000)$ ($h\ m\ s\ \pm\ s$)	$\delta(J2000)$ ($^\circ\ ' \ ''\ \pm\ ''$)
(1)	(2)	(3)	(4)	(5)	(6)	(7)	(8)
NGC 185	S2	dE3 pec	-5.0	10.10	0.7	00 38 57.40 \pm 0.27	+48 20 14.4 \pm 2.7
NGC 676	S2:	S0/a: spin	0.0	10.50	19.5	01 48 57.38 \pm 0.11	+05 54 25.7 \pm 1.7
NGC 777	S2/L2::	E1	-5.0	12.49	66.5	02 00 15.01 \pm 0.16	+31 25 45.5 \pm 2.1
NGC 1058	S2	Sc	5.0	11.82	9.1	02 43 30.24 \pm 0.22	+37 20 27.2 \pm 2.6
NGC 1068	S1.9	Sb	3.0	9.61	14.4	02 42 40.737 \pm 0.006	-00 00 47.65 \pm 0.09
NGC 1167	S2	S0-	-3.0	13.38	65.3	03 01 42.369 \pm 0.010	+35 12 20.68 \pm 0.13
NGC 1275	S1.5	Pec	99.0	12.64	70.1	03 19 48.161 \pm 0.007	+41 30 42.38 \pm 0.08
NGC 1358	S2	SAB0/a	0.0	13.04	53.6	03 33 39.673 \pm 0.011	-05 05 21.85 \pm 0.17
NGC 1667	S2	SABc	5.0	12.77	61.2	04 48 37.141 \pm 0.013	-06 19 11.88 \pm 0.19
NGC 2273	S2	SBA:	0.5	12.55	28.4	06 50 08.717 \pm 0.018	+60 50 45.01 \pm 0.13
NGC 2639	S1.9	Sa?	1.0	12.56	42.6	08 43 38.000 \pm 0.012	+50 12 20.32 \pm 0.10
NGC 2655	S2	SAB0/a	0.0	10.96	24.4	08 55 38.84 \pm 0.55	+78 13 25.2 \pm 1.7
NGC 2685	S2/T2:	SB0+ pec	-1.0	12.12	16.2	08 55 34.79 \pm 0.39	+58 44 01.6 \pm 3.1
NGC 3031	S1.5	Sab	2.0	7.89	1.4	09 55 33.173 \pm 0.023	+69 03 55.06 \pm 0.12
NGC 3079	S2	Sbc spin	7.0	11.54	20.4	10 01 58.53 \pm 0.63	+55 40 50.1 \pm 5.4
NGC 3147	S2	Sbc	4.0	11.43	40.9	10 16 53.27 \pm 0.72	+73 24 02.4 \pm 3.1
NGC 3185	S2:	SB0/a	1.0	12.99	21.3	10 17 38.66 \pm 0.12	+21 41 17.2 \pm 1.7
NGC 3227	S1.5	SABa pec	1.0	11.10	20.6	10 23 30.589 \pm 0.007	+19 51 53.99 \pm 0.10
NGC 3254	S2	Sbc	4.0	12.41	23.6	10 29 19.96 \pm 0.13	+29 29 29.6 \pm 1.7
NGC 3486	S2	SABc	5.0	11.05	7.4	11 00 24.10 \pm 0.20	+28 58 31.6 \pm 2.7
NGC 3516	S1.2	SB0:	-2.0	12.50	38.9	11 06 47.490 \pm 0.023	+72 34 06.88 \pm 0.10
NGC 3735	S2:	Sc: spin	5.0	12.50	41.0	11 35 57.49 \pm 0.57	+70 32 07.7 \pm 2.8
NGC 3941	S2:	SB0	-2.0	11.25	18.9	11 52 55.42 \pm 0.21	+36 59 10.5 \pm 2.5
NGC 3976	S2:	SABb	3.0	12.30	37.7	11 55 57.35 \pm 0.17	+06 44 57.0 \pm 2.5
NGC 3982	S1.9	SABb:	3.0	11.78	17.0	11 56 28.102 \pm 0.012	+55 07 30.58 \pm 0.12
NGC 4051	S1.2	SABbc	4.0	10.83	17.0	12 03 09.614 \pm 0.013	+44 31 52.80 \pm 0.14
NGC 4138	S1.9	S0+	-1.0	12.16	17.0	12 09 29.87 \pm 0.19	+43 41 06.0 \pm 2.1
NGC 4151	S1.5	SABab:	2.0	11.50	20.3	12 10 32.579 \pm 0.009	+39 24 20.63 \pm 0.10
NGC 4168	S1.9:	E2	-5.0	12.11	16.8	12 12 17.30 \pm 0.14	+13 12 17.9 \pm 2.1
NGC 4169	S2	S0	-2.0	13.15	50.4	12 12 18.93 \pm 0.12	+29 10 44.0 \pm 1.6
NGC 4203 ^a	L1.9	SAB0-	-3.0	11.80	9.7	12 15 04.98 \pm 0.19	+33 11 49.8 \pm 2.4
NGC 4235	S1.2	Sa spin	1.0	12.62	35.1	12 17 09.904 \pm 0.008	+07 11 29.08 \pm 0.12
NGC 4258	S1.9	SABbc	4.0	9.10	6.8	12 18 57.54 \pm 0.60	+47 18 14.3 \pm 6.1
NGC 4378	S2	Sa	1.0	12.63	35.1	12 25 18.14 \pm 0.15	+04 55 31.6 \pm 2.3
NGC 4388	S1.9	Sb: spin	3.0	11.76	16.8	12 25 46.701 \pm 0.009	+12 39 40.92 \pm 0.13
NGC 4395	S1.8	Sm:	9.0	10.64	3.6	12 25 48.93 \pm 0.11	+33 32 47.8 \pm 1.3
NGC 4450 ^a	L1.9	Sab	2.0	10.90	16.8	12 28 29.64 \pm 0.12	+17 05 04.8 \pm 1.7
NGC 4472	S2::	E2	-5.0	9.37	16.8	12 29 46.76 \pm 0.15	+07 59 59.9 \pm 2.2
NGC 4477	S2	SB0?	-2.0	11.38	16.8	12 30 02.22 \pm 0.18	+13 38 11.3 \pm 2.6
NGC 4501	S2	Sb	3.0	10.36	16.8	12 31 59.34 \pm 0.18	+14 25 13.4 \pm 2.7
NGC 4565	S1.9	Sb? spin	3.0	10.42	9.7	12 36 21.07 \pm 0.70	+25 59 13.5 \pm 9.4
NGC 4579	S1.9/L1.9	SABb	3.0	10.48	16.8	12 37 43.532 \pm 0.011	+11 49 04.91 \pm 0.16
NGC 4639	S1.0	SABbc	4.0	12.24	16.8	12 42 52.51 \pm 0.16	+13 15 24.1 \pm 2.3
NGC 4698	S2	Sab	2.0	11.46	16.8	12 48 22.98 \pm 0.16	+08 29 14.8 \pm 2.4
NGC 4725	S2:	SABab pec	2.0	10.11	12.4	12 50 26.69 \pm 0.16	+25 30 02.3 \pm 2.2
NGC 5033	S1.5	Sc	5.0	10.75	18.7	13 13 27.523 \pm 0.010	+36 35 37.78 \pm 0.12
NGC 5194	S2	Sbc pec	4.0	8.96	7.7	13 29 52.37 \pm 0.26	+47 11 40.8 \pm 2.7
NGC 5273	S1.5	S0	-2.0	12.44	21.3	13 42 08.338 \pm 0.009	+35 39 15.17 \pm 0.11
NGC 5395	S2/L2	Sb pec	3.0	12.10	46.7	13 58 38.01 \pm 0.18	+37 25 28.3 \pm 2.2
NGC 5548	S1.5	S0/a	0.0	13.30	67.0	14 17 59.534 \pm 0.010	+25 08 12.44 \pm 0.14
NGC 5631	S2/L2:	S0	-2.0	12.41	32.7	14 26 33.27 \pm 0.21	+56 34 58.3 \pm 1.7
NGC 6951	S2	SABbc	4.0	11.64	24.1	20 37 14.41 \pm 0.44	+66 06 19.7 \pm 2.7
NGC 7479	S1.9	Sbc	5.0	11.60	32.4	23 04 56.69 \pm 0.20	+12 19 23.2 \pm 2.9
NGC 7743	S2	SB0+	-1.0	12.38	24.4	23 44 21.44 \pm 0.13	+09 56 03.6 \pm 1.9

^aNot formally part of the Seyfert sample.

TABLE 2: OBSERVATIONAL SUMMARY

Parameter	Session 1	Session 2
Date	1999 August 29	1999 October 31
Configuration	A	B
Maximum number antennas	24	27
Length of observations (hr)	22	23
Frequency (GHz)	1.4250	4.8601
Bandwidth (MHz)	100	100
Theoretical noise (mJy/beam)	0.04	0.04
Primary flux calibrator	3C 286	3C 286
Assumed flux of primary flux calibrator (Jy)	14.75	7.49
Polarization leakage calibrator	1313+675	1313+675
Largest angular scale (arcmin)	1	1
HPBW primary antenna beam (arcmin)	28.1	8.4
HPBW synthesized beam, uniform weight (arcsec)	1.1	1.1
HPBW synthesized beam, tapered, natural weight (arcsec)	2.5/3.6	2.5/3.6

TABLE 3: RADIO MEASUREMENTS

Galaxy	Fig.	MAP PARAMETERS				SOURCE PARAMETERS										P.A.	$S_{\text{pol},6}^P$ ^a	$S_{\text{pol},20}^P$ ^a
		Beam ($'' \times ''$) (3)	P.A. (deg.) (4)	rms(6) (mJy) ^b (5)	rms(20) (mJy) (6)	α (J2000) (h m s) (7)	δ (J2000) ($^{\circ}$ ' $''$) (8)	S_6^P (mJy) (9)	S_6^I (mJy) (10)	S_{20}^P (mJy) (11)	S_{20}^I (mJy) (12)	α_6^{20} (13)	$\theta_M \times \theta_m$ ($'' \times ''$) (14)					
(1)	(2)	(3)	(4)	(5)	(6)	(7)	(8)	(9)	(10)	(11)	(12)	(13)	(14)	(15)	(16)	(17)		
NGC 185	2	1.31×1.18	159	0.041	0.042	<0.12	...	<0.13		
		2.46×2.42	164	0.044	0.041	<0.13	...	<0.12		
NGC 676	2	1.22×1.17	95	0.062	0.044	<0.18	...	<0.13		
		2.56×2.39	1	0.084	0.044	<0.25	...	<0.13		
NGC 777	2	1.19×1.01	144	0.061	0.095	02 00 14.900	+31 25 46.00	1.43	2.63	1.99	3.19	-0.16	<0.60×0.51	...	<0.082	<0.078		
		2.46×2.42	59	0.055	0.048	02 00 14.900	+31 25 45.80	1.95	2.86	4.00	5.25		
NGC 1058	2	1.16×0.97	149	0.039	0.041	<0.12	...	<0.12		
		2.44×2.43	62	0.048	0.036	<0.14	...	<0.11		
NGC 1068	3, 16a	1.31×1.27	3	0.14	0.18	02 42 40.73	-00 00 47.7	518	1650	1250	3960	-0.71		
		core+lobe				02 42 40.73	-00 00 47.7	518	1560	1250	3890	-0.74	2.38	0.82		
		core				02 42 40.723	-00 00 47.55	524	644	1240	1630	-0.76	0.88×0.26	29		
		2.95×2.33	86	0.089	0.19	02 42 40.71	-00 00 47.7	601	1570	1470	3860		
NGC 1167	3, 16b	1.22×1.10	151	0.037	0.052	03 01 42.360	+35 12 20.10	566	926	1189	1756	-0.52	1.29×0.57	117	0.81	1.09		
		2.45×2.43	59	0.035	0.035	03 01 42.356	+35 12 20.16	773	927	1510	1830		
NGC 1275	3, 16c	1.25×1.09	152	0.10	0.79	03 19 48.16	+41 30 42.1	20600	20700	21900	23200	-0.09		
		core				03 19 48.160	+41 30 42.11	20600	20600	21900	22000	-0.05	<0.63×0.55	...	9.99	20.5		
		2.45×2.43	156	0.55	2.6	03 19 48.16	+41 30 42.1	20600	20800	22000	22900		
NGC 1358	3	1.30×1.19	13	0.049	0.053	03 33 39.69	-05 05 22.1	1.22	7.04	1.75	17.9	-0.76	<0.077	<0.089		
		core				03 33 39.684	-05 05 22.17	1.23	1.42	1.68	2.81	-0.56	<0.65×0.60		
		2.81×2.36	159	0.068	0.039	03 33 39.67	-05 05 22.5	1.44	10.6	1.96	7.89		
NGC 1667	4	1.44×1.20	164	0.058	0.052	04 48 37.179	-06 19 11.71	1.17	1.19	3.25	4.08	-1.00	<0.72×0.60	...	<0.084	<0.082		
		2.95×2.35	151	0.065	0.030	04 48 37.18	-06 19 11.9	1.22	21.6	3.26	7.98		
NGC 2273	4	1.42×0.96	37	0.064	0.049	06 50 08.649	+60 50 45.01	14.2	24.5	29.1	47.3	-0.54	1.12×0.61	84	<0.092	<0.081		
		2.74×2.36	38	0.056	0.23	06 50 08.635	+60 50 45.01	19.8	26.7	42.3	53.7		
NGC 2639	4, 16e	1.46×0.98	61	0.066	0.048	08 43 38.08	+50 12 20.0	173	186	78.9	103	0.48		
		core				08 43 38.076	+50 12 20.00	173	182	79.7	102	0.47	<0.73×0.49	...	0.22	<0.086		
		2.66×2.39	82	0.14	0.037	08 43 38.076	+50 12 20.01	180	184	96.1	103		
NGC 2655	4, 16h	3.00×0.90	19	0.067	0.070	08 55 37.95	+78 13 23.7	34.4	44.1	79.8	101	-0.68	0.20	0.25		
		core				08 55 37.974	+78 13 23.69	34.4	38.8	79.8	92.3	-0.71	<1.50×0.45		
		4.48×2.30	17	0.038	0.081	08 55 37.95	+78 13 23.4	37.8	46.1	90.5	110		
		core				08 55 37.971	+78 13 23.69	38.1	40.0	90.7	96.2		
NGC 2685	5	1.50×0.94	58	0.044	0.045	<0.13	...	<0.14		
		2.70×2.38	72	0.038	0.043	<0.11	...	<0.13		
NGC 3031 ^c	5, 16d	1.01×0.91	89	0.029	0.028	09 55 33.18	+69 03 55.1	84.4	91.2	69.5	79.2	0.12		
		core				09 55 33.182	+69 03 55.09	87.3	90.4	72.2	76.4	0.14	<0.50×0.45		
		2.86×2.43	91	0.025	0.020	09 55 33.20	+69 03 55.1	90.0	94.0	76.2	84.0		
		core				09 55 33.181	+69 03 55.09	90.2	91.6	76.2	79.2		
		“arc”				09 55 39.2	+69 04 27	0.12	2.47	1.14	2.46	0.12	0.096		
NGC 3079	5, 16g	1.58×0.97	69	0.093	0.15	10 01 57.79	+55 40 47.8	92.4	189	75.4	275	-0.31	0.41	<0.096		
		core				10 01 57.787	+55 40 47.51	90.1	114	70.2	132	-0.12	<0.79×0.49		
		2.95×2.33	86	0.089	0.20	10 01 57.79	+55 40 47.7	110	182	115	254		
NGC 3147	5, 16f	3.56×0.89	27	0.070	0.055	10 16 53.655	+73 24 02.72	10.1	10.1	13.3	13.6	-0.24	<1.78×0.45	...	0.23	<0.11		
		5.14×2.36	26	0.039	0.041	10 16 53.657	+73 24 02.73	10.0	10.0	13.8	13.9		
NGC 3185	6	1.46×1.22	87	0.052	0.052	10 17 38.66	+21 41 17.4	0.19	0.47	<0.16	<0.081	...		
		2.90×2.35	119	0.050	0.037	10 17 38.575	+21 41 17.36	0.50	1.92	<0.11	5.70×3.28	137		
NGC 3227	6	1.39×1.19	81	0.056	0.049	10 23 30.579	+19 51 54.33	20.1	25.9	58.2	78.2	-0.90	0.73×0.62	2	<0.082	<0.089		
		2.84×2.36	121	0.052	0.056	10 23 30.59	+19 51 54.6	23.8	31.3	70.0	81.2		

TABLE 3: RADIO MEASUREMENTS—*Continued*

MAP PARAMETERS						SOURCE PARAMETERS											
Galaxy	Fig.	Beam ($'' \times ''$)	P.A. (deg.)	rms(6) (mJy) ^b	rms(20) (mJy)	α (J2000) (h m s)	δ (J2000) ($^{\circ}$ ' $''$)	S_6^P (mJy)	S_6^I (mJy)	S_{20}^P (mJy)	S_{20}^I (mJy)	α_6^{20}	$\theta_M \times \theta_m$ ($'' \times ''$)	P.A. (deg.)	$S_{\text{pol},6}^P$ ^a (mJy)	$S_{\text{pol},20}^P$ ^a (mJy)	
(1)	(2)	(3)	(4)	(5)	(6)	(7)	(8)	(9)	(10)	(11)	(12)	(13)	(14)	(15)	(16)	(17)	
NGC 3254	6	1.33×1.15	62	0.040	0.040	<0.12	...	<0.12	
		2.62×2.41	108	0.047	0.032	<0.14	...	<0.10	
NGC 3486	6	1.32×1.10	75	0.040	0.041	<0.12	...	<0.12	
		2.65×2.39	109	0.051	0.035	<0.15	...	<0.11	
NGC 3516	7	3.58×0.91	32	0.056	0.075	11 06 47.49	+72 34 07.4	3.22	6.03	5.62	29.8	-1.30	<0.091	<0.12	
		core				11 06 47.492	+72 34 07.46	3.05	3.93	5.02	8.95	-0.67	1.71×0.49	23	
		5.05×2.32	33	0.039	0.073	11 06 47.49	+72 34 07.5	3.94	12.2	7.11	13.1	
NGC 3735	7	3.84×0.89	34	0.077	0.066	11 35 57.265	+70 32 08.04	0.81	1.24	0.79	1.61	-0.21	<1.92×0.45	...	<0.092	<0.11	
		6.12×3.42	29	0.063	0.043	11 35 57.30	+70 32 08.2	1.52	21.0	1.55	14.1	
NGC 3941	7	1.35×1.05	122	0.048	0.045	11 52 55.363	+36 59 10.89	0.23	0.19	<0.14	<0.68×0.53	...	<0.073	...	
		2.58×2.40	80	0.045	0.042	11 52 55.369	+36 59 11.02	0.27	0.33	<0.13	
NGC 3976	7	1.61×1.32	117	0.039	0.059	11 55 57.275	+06 44 57.28	0.45	0.41	<0.18	<0.81×0.66	...	<0.073	...	
		3.20×2.35	121	0.055	0.051	11 55 57.267	+06 44 57.45	0.49	0.53	<0.15	
NGC 3982	8	1.97×0.97	88	0.048	0.069	11 56 28.142	+55 07 30.83	1.77	1.79	2.90	3.56	-0.56	<0.99×0.49	...	<0.084	<0.10	
		4.11×2.17	69	0.042	0.11	11 56 28.20	+55 07 31.2	1.59	4.18	2.89	3.47	
NGC 4051	8	1.42×1.05	122	0.049	0.043	12 03 09.61	+44 31 52.8	2.15	6.38	4.29	14.7	-0.68	<0.080	<0.087	
		core				12 03 09.613	+44 31 52.65	2.05	3.21	4.00	7.35	-0.68	0.99×0.80	68	
		2.60×2.40	91	0.056	0.031	12 03 09.61	+44 31 52.8	3.29	9.94	6.72	14.2	
NGC 4138	8	1.42×1.02	113	0.047	0.067	12 09 29.789	+43 41 06.91	0.78	0.78	0.51	0.45	0.45	<0.71×0.51	...	<0.092	<0.090	
		2.64×2.40	88	0.061	0.20	12 09 29.83	+43 41 06.5	0.56	0.31	<0.60	
NGC 4151	8, 16j	1.61×1.04	96	0.068	0.061	12 10 32.56	+39 24 21.1	81.3	139	174	347	-0.75	
		core				12 10 32.556	+39 24 21.00	77.6	129	175	324	-0.75	1.84×0.33	76	0.30	0.31	
		3.97×3.57	76	0.053	0.063	12 10 32.58	+39 24 21.1	116	142	275	351	
NGC 4168	9	1.23×1.18	78	0.058	0.050	12 12 17.268	+13 12 18.63	5.01	5.24	4.02	4.37	0.15	<0.62×0.59	...	<0.083	<0.081	
		2.71×2.39	135	0.050	0.033	12 12 17.269	+13 12 18.64	5.13	5.15	4.27	4.50	
NGC 4169	9	1.20×1.03	38	0.055	0.044	12 12 18.76	+29 10 45.8	0.19	0.30	0.21	0.89	-0.89	<0.078	<0.078	
		2.50×2.44	0	0.058	0.041	12 12 18.778	+29 10 46.01	0.31	0.62	0.25	0.22	...	3.46×1.38	110	
NGC 4203	9	1.18×1.01	36	0.046	0.054	12 15 05.055	+33 11 50.36	10.4	11.2	5.82	6.52	0.44	<0.59×0.51	...	<0.082	<0.086	
		2.45×2.44	79	0.038	0.041	12 15 05.04	+33 11 50.3	10.9	11.3	6.26	6.46	
NGC 4235	9	1.64×1.30	112	0.055	0.040	12 17 09.881	+07 11 29.64	5.08	5.61	3.37	5.05	0.09	<0.82×0.65	...	<0.085	<0.085	
		3.21×2.36	122	0.050	0.039	12 17 09.879	+07 11 29.64	5.43	5.81	4.22	5.52	
NGC 4258	10	1.47×0.98	113	0.065	0.043	12 18 57.49	+47 18 14.2	1.76	2.40	1.73	7.95	-0.98	<0.086	<0.094	
		core				12 18 57.506	+47 18 14.28	1.74	2.18	1.60	2.73	-0.18	0.80×0.36	149	
		2.67×2.40	91	0.11	0.038	12 18 57.504	+47 18 14.39	1.93	3.52	2.43	6.53	
NGC 4378	10	1.30×1.19	13	0.049	0.041	12 25 18.082	+04 55 30.43	0.30	0.21	<0.12	<0.65×0.62	...	<0.085	...	
		3.15×2.36	128	0.057	0.030	12 25 18.076	+04 55 30.64	0.22	0.45	<0.09	
NGC 4388	10	1.14×1.11	47	0.044	0.052	12 25 46.79	+12 39 43.7	5.43	26.9	12.9	44.3	-0.41	<0.076	<0.086	
		core-N				12 25 46.781	+12 39 43.71	5.02	7.86	7.22	11.6	-0.32	1.12×0.55	36	
		core-S				12 25 46.730	+12 39 41.91	3.95	9.04	11.7	24.2	-0.80	1.43×1.12	6	
		2.51×2.41	73	0.11	0.058	12 25 46.74	+12 39 42.7	10.4	45.7	22.7	38.8	
NGC 4395	10	1.66×1.10	90	0.056	0.043	12 25 48.872	+33 32 48.80	0.68	0.80	1.54	1.68	-0.60	<0.83×0.55	...	<0.082	<0.088	
		3.10×2.33	71	0.051	0.083	12 25 48.888	+33 32 48.71	0.84	1.26	1.79	1.99	
NGC 4450	11	1.13×1.10	16	0.058	0.038	12 28 29.592	+17 05 05.95	5.91	6.49	4.36	5.99	0.07	<0.57×0.55	...	<0.083	<0.089	
		2.48×2.41	3	0.052	0.032	12 28 29.590	+17 05 05.98	6.45	6.75	5.67	6.33	
NGC 4472	11, 16l	1.48×1.24	103	0.062	0.049	12 29 46.750	+08 00 01.54	19.1	65.2	32.3	113	-0.45	3.42×1.09	76	1.26	0.39	
		2.92×2.38	131	0.071	0.033	12 29 46.75	+08 00 01.5	36.5	68.1	61.5	110	
NGC 4477	11	1.15×1.11	144	0.044	0.041	12 30 02.26	+13 38 12.5	0.17	0.18	<0.12	<0.57×0.56	...	<0.081	...	
		3.73×3.61	16	0.056	0.081	12 30 02.20	+13 38 12.75	0.25	0.26	<0.24	

TABLE 3: RADIO MEASUREMENTS—*Continued*

MAP PARAMETERS						SOURCE PARAMETERS										
Galaxy	Fig.	Beam ($'' \times ''$) (3)	P.A. (deg.) (4)	rms(6) (mJy) ^b (5)	rms(20) (mJy) (6)	α (J2000) (h m s) (7)	δ (J2000) ($^{\circ}$ ' ") (8)	S_6^P (mJy) (9)	S_6^I (mJy) (10)	S_{20}^P (mJy) (11)	S_{20}^I (mJy) (12)	α_6^{20} (13)	$\theta_M \times \theta_m$ ($'' \times ''$) (14)	P.A. (deg.) (15)	$S_{\text{pol},6}^P$ ^a (mJy) (16)	$S_{\text{pol},20}^P$ ^a (mJy) (17)
(1)	(2)	(3)	(4)	(5)	(6)	(7)	(8)	(9)	(10)	(11)	(12)	(13)	(14)	(15)	(16)	(17)
NGC 4501	11	1.16×1.08	145	0.062	0.046	12 31 59.153	+14 25 13.12	1.06	1.14	1.81	2.06	−0.48	<0.58×0.54	...	<0.082	<0.088
		2.50×2.40	17	0.065	0.038	12 31 59.147	+14 25 13.07	1.09	1.04	1.83	1.78
NGC 4565	12	1.18×1.03	34	0.057	0.039	12 36 20.781	+25 59 15.64	2.61	2.72	2.05	2.31	0.13	<0.59×0.52	...	<0.080	<0.084
		2.47×2.43	128	0.053	0.035	12 36 20.778	+25 59 15.68	2.64	2.67	2.21	2.66
NGC 4579	12	1.17×1.07	142	0.059	0.059	12 37 43.52	+11 49 05.50	38.0	43.1	18.6	27.8	0.36	<0.076	<0.086
		core				12 37 43.525	+11 49 05.49	37.7	39.4	18.9	22.3	0.46	<0.59×0.54
		2.53×2.40	20	0.071	0.068	12 37 43.525	+11 49 05.53	39.3	42.8	21.8	28.2
NGC 4639	12	1.18×1.07	143	0.050	0.043	12 42 52.363	+13 15 26.75	0.22	0.15	<0.13	<0.59×0.54	...	<0.082	...
		2.52×2.40	25	0.051	0.043	12 42 52.341	+13 15 26.77	0.21	0.59	<0.13
NGC 4698	12	1.25×1.11	142	0.055	0.043	12 48 22.919	+08 29 14.55	0.26	0.23	<0.13	<0.63×0.56	...	<0.079	...
		2.57×2.39	26	0.072	0.032	12 48 22.897	+08 29 14.92	0.37	0.31	<0.10
NGC 4725	13	1.17×1.03	34	0.058	0.039	<0.17	...	<0.12
		2.46×2.43	133	0.051	0.045	<0.15	...	<0.14
NGC 5033	13	1.68×1.09	90	0.059	0.054	13 13 27.46	+36 35 37.8	3.02	5.68	5.74	11.7	−0.59	<0.084	<0.098
		core				13 13 27.475	+36 35 37.94	2.95	4.20	5.38	7.99	−0.52	0.94×0.80	92
		4.03×3.57	69	0.073	0.079	13 13 27.53	+36 35 38.1	4.55	24.1	8.16	16.1
NGC 5194	13, 16i	2.02×1.03	83	0.057	0.060	13 29 52.69	+47 11 42.8	0.98	13.7	2.09	26.8	−0.55	0.17	0.24
		core				13 29 52.696	+47 11 42.72	0.98	1.31	1.68	3.43	−0.78	<1.01×0.52
		3.37×2.34	74	0.13	0.043	13 29 52.76	+47 11 39.4	2.43	21.0	6.09	26.1
NGC 5273	13	1.66×1.04	92	0.060	0.049	13 42 08.370	+35 39 15.33	1.01	1.31	1.88	2.13	−0.40	<0.83×0.52	...	<0.083	<0.098
		3.08×2.35	72	0.046	0.038	13 42 08.380	+35 39 15.34	1.26	1.77	2.27	2.55
NGC 5395	14	2.19×1.07	78	0.064	0.049	<0.19	...	<0.15
		3.62×2.34	67	0.068	0.13	<0.20	...	<0.39
NGC 5548	14, 16k	1.62×1.16	87	0.058	0.052	14 17 59.53	+25 08 12.7	2.67	9.90	4.67	19.8	−0.56	0.17	0.24
		core				14 17 59.535	+25 08 12.63	2.65	2.89	4.62	5.06	−0.46	<0.81×0.58
		3.13×2.33	67	0.072	0.054	14 17 59.53	+25 08 12.4	3.14	12.3	5.55	22.6
NGC 5631	14	3.24×0.96	63	0.068	0.066	14 26 33.299	+56 34 57.47	0.37	0.29	0.29	0.43	−0.32	<1.62×0.48	...	<0.092	<0.11
		4.68×2.31	60	0.056	0.059	14 26 33.286	+56 34 57.62	0.29	0.30	<0.18
NGC 6951	14	1.43×0.94	155	0.055	0.047	20 37 14.14	+66 06 19.9	0.99	9.05	2.53	25.5	−0.84	<0.082	<0.087
		core				20 37 14.118	+66 06 20.02	1.01	1.22	2.36	3.66	−0.90	<0.72×0.47
		2.60×2.40	157	0.051	0.049	20 37 13.58	+66 06 23.3	1.74	14.7	3.19	23.4
NGC 7479	15, 16m	1.19×1.11	36	0.057	0.044	23 04 56.827	+12 19 21.10	2.69	3.07	3.28	10.5	−1.00	0.16	0.10
		core				23 04 56.827	+12 19 21.10	2.69	3.07	3.20	3.96	−0.21	<0.59×0.56
		2.51×2.41	168	0.069	0.039	23 04 56.84	+12 19 20.9	3.25	11.3	3.79	8.63
NGC 7743 ^d	15	3.86×3.66	1	0.088	0.049	23 44 21.16	+09 56 03.6	2.81	3.03	4.86	5.52	−0.49
		6.69×6.15	177	0.053	...	23 44 21.19	+09 56 03.2	2.79	3.05
		1.36×1.28	168	...	0.058	23 44 21.16	+09 56 03.4	3.33	5.01	...	1.29×0.53	33

^aAppendix B gives additional details of the polarization maps for the objects with detected polarizations.^b“mJy” denotes mJy beam^{−1}.^cArchival data, based on observations by Kaufman et al. 1996.^dArchival data, based on 6 cm C-array observations by Wrobel & Heeschen 1991 and 20 cm A-array observations by Nagar et al. 1999.

TABLE 4: BACKGROUND SOURCES

Galaxy	S_6^I (mJy)	S_{20}^I (mJy)	$\alpha(J2000)$ (h m s)	$\delta(J2000)$ ($^{\circ}$ ' ")	Galaxy	S_6^I (mJy)	S_{20}^I (mJy)	$\alpha(J2000)$ (h m s)	$\delta(J2000)$ ($^{\circ}$ ' ")
NGC 185	...	55	00 38 20.6	+48 28 22	NGC 4395	5.7	22	12 25 59.7	+33 33 40
...	...	5.0	00 39 17.5	+48 12 17	...	1.3	3.3	12 25 50.7	+33 34 19
NGC 676	300	674	01 49 22.3	+05 55 54	...	1.9	2.1	12 25 49.8	+33 29 47
NGC 777	13	66	02 00 20.3	+31 22 20	5.3	12 24 58.5	+33 28 23
...	...	210	01 59 45.7	+31 23 04	15	12 24 56.5	+33 28 17
NGC 1058	...	47	02 44 25.4	+37 17 51	NGC 4450	3.9	2.6	12 28 35.1	+17 05 13
NGC 1161	...	169	03 02 12.9	+35 08 22	...	1.6	8.4	12 28 13.9	+17 06 37
NGC 1358	1.1	...	03 33 36.9	-05 08 31	...	1.8	9.2	12 28 18.6	+17 03 50
...	...	16	03 33 18.2	-05 08 19	...	2.2	11	12 28 17.4	+17 03 43
...	...	56	03 32 48.4	-05 00 19	9.7	12 28 58.7	+17 10 35
...	...	22	03 32 46.6	-05 06 22	NGC 4472	...	46	12 29 59.7	+07 51 53
NGC 1667	1.9	13	04 48 50.6	-06 15 37	...	64	12 29 47.6	+07 50 31	
...	1.5	5.5	04 48 22.9	-06 19 01	NGC 4477	0.3	...	12 30 11.9	+13 38 27
...	...	8.9	04 49 06.7	-06 17 34	...	0.4	...	12 29 58.9	+13 40 12
...	...	19	04 49 13.4	-06 25 02	...	1.2	...	12 29 52.5	+13 39 58
...	...	15	04 48 28.6	-06 26 37	223	12 29 59.5	+13 27 59
...	...	23	04 48 15.8	-06 29 55	6.4	12 29 51.5	+13 36 23
NGC 2273	23	15	06 50 12.8	+60 48 42	NGC 4501	1.0	...	12 31 56.8	+14 22 24
...	...	8.3	06 49 58.7	+60 44 32	24	12 32 21.7	+14 24 19
NGC 2639	...	39	08 43 48.2	+50 15 39	33	12 31 24.3	+14 21 27
...	...	38	08 43 27.7	+50 23 33	NGC 4565	1.6	15	12 36 36.2	+26 02 13
NGC 2655	...	29	09 01 18.5	+78 13 05	56	12 35 23.3	+25 56 29
...	...	38	08 53 13.7	+78 03 12	16	12 35 50.1	+26 09 49
NGC 3079	...	35	10 00 59.5	+55 40 57	NGC 4579	...	6.6	12 38 00.6	+11 53 51
...	...	44	10 02 10.1	+55 51 27	4.7	12 38 21.5	+11 59 18
NGC 3147	...	3.3	10 17 57.2	+73 25 18	40	12 36 49.3	+11 47 58
...	...	27	10 18 27.8	+73 19 13	2.5	12 37 06.5	+11 42 30
...	...	2.4	10 17 47.3	+73 17 55	NGC 4639	...	33	12 43 40.8	+13 15 45
NGC 3185	0.3	...	10 17 38.5	+21 43 01	29	12 42 28.2	+13 04 21
...	2.7	...	10 17 31.8	+21 37 36	NGC 4698	0.8	...	12 48 25.9	+08 30 21
...	...	23	10 17 57.6	+21 36 29	...	0.5	...	12 48 15.1	+08 30 19
...	...	44	10 16 55.4	+21 32 18	...	0.3	...	12 48 33.6	+08 30 22
...	...	7.9	10 17 04.7	+21 34 47	85	12 48 06.4	+08 22 38
NGC 3227	5.7	3.8	10 23 27.0	+19 53 54	5.1	12 48 08.3	+08 32 05
NGC 3254	...	11	10 29 24.9	+29 24 01	NGC 4725	0.6	4.6	12 50 40.9	+25 28 19
...	...	3.0	10 29 05.9	+29 25 26	...	0.5	1.9	12 50 12.8	+25 30 36
...	...	75	10 28 37.6	+29 22 51	51	12 49 32.8	+25 33 04
...	...	8.7	10 29 27.9	+29 37 46	NGC 5033	0.8	...	13 13 10.2	+36 34 43
NGC 3486	...	4.2	11 00 04.4	+29 00 27	...	0.7	...	13 13 33.4	+36 37 29
...	...	7.2	11 00 55.5	+28 48 58	...	0.3	...	13 13 24.8	+36 35 04
NGC 3516	122	326	11 07 41.7	+72 32 37	...	0.2	...	13 13 30.1	+36 35 37
NGC 3735	...	18	11 36 24.7	+70 43 18	205	13 14 43.1	+36 38 59
NGC 3941	...	28	11 52 16.6	+37 05 44	NGC 5194	3.0	13	13 30 05.1	+47 10 36
...	...	3.4	11 52 52.2	+37 05 05	...	0.5	...	13 30 01.5	+47 12 51
NGC 3976	...	83	11 56 59.8	+06 41 16	13	13 30 16.3	+47 10 30
NGC 3982	2.7	13	11 55 58.6	+55 11 07	4.9	13 29 59.5	+47 15 57
...	...	421	11 57 19.8	+54 57 47	NGC 5273	...	39	13 41 33.6	+35 32 57
...	...	37	11 55 13.8	+55 04 47	4.1	13 41 11.6	+35 43 20
NGC 4051	0.9	3.2	12 03 10.2	+44 28 15	NGC 5395	10	25	13 58 33.8	+37 27 17
...	6.3	23	12 03 26.4	+44 36 34	...	0.6	...	13 58 47.9	+37 24 03
...	...	2.8	12 04 01.3	+44 38 00	NGC 5548	2.9	18	14 18 17.4	+25 07 25
NGC 4138	419	1270	12 09 13.4	+43 39 17	...	9.3	27	14 17 51.9	+25 08 19
...	...	325	12 09 14.2	+43 39 25	3.5	14 17 55.8	+25 08 07
NGC 4168	...	325	12 13 30.9	+13 07 25	15	14 18 32.6	+25 12 02
NGC 4169	7.8	35	12 12 30.9	+29 10 07	5.7	14 17 26.6	+25 06 30
...	...	28	12 11 47.9	+29 18 20	NGC 5631	11	39	14 26 33.9	+56 37 59
NGC 4203	2.6	...	12 15 14.3	+33 11 05	45	14 27 58.8	+56 32 56
...	...	705	12 14 04.9	+33 09 47	NGC 6951	0.3	...	20 37 24.7	+66 05 16
NGC 4235	2.7	2.0	12 17 10.3	+07 14 17	19	20 36 53.3	+66 16 32
...	...	7.8	12 17 55.4	+07 13 03	NGC 7479	0.8	1.5	23 04 58.7	+12 19 17
NGC 4258	...	4.3	12 19 32.5	+47 18 21	...	1.6	2.5	23 04 55.4	+12 20 59
...	...	3.5	12 18 46.3	+47 14 20	12	23 04 31.2	+12 16 52
NGC 4378	0.4	...	12 25 26.0	+04 55 23	4.5	23 04 32.2	+12 23 12
...	0.5	...	12 25 11.1	+04 57 47	6.2	23 04 46.4	+12 24 26
...	...	0.5	12 25 22.1	+04 58 28	NGC 7743	2.1	6.8	23 44 30.7	+09 51 33
...	...	9.1	12 25 19.3	+05 00 36	...	0.7	...	23 44 15.5	+10 00 42
...	...	1.4	12 25 24.2	+04 50 49	150	23 43 42.7	+10 01 22

TABLE 5: SUMMARY

Galaxy	RADIO PROPERTIES								OPTICAL PROPERTIES				
	$\log P_6^{\text{core}}$ (W Hz ⁻¹)	$\log P_6^{\text{tot}}$ (W Hz ⁻¹)	$\log P_{20}^{\text{core}}$ (W Hz ⁻¹)	$\log P_{20}^{\text{tot}}$ (W Hz ⁻¹)	Θ ($''$)	L (pc)	P.A._{rad} (deg.)	Morph.	$M_{B_T}^0$ (mag)	P.A._{opt} (deg.)	$\log L(\text{[O III]})$ (erg s ⁻¹)	$\log L(\text{H}\alpha)$ (erg s ⁻¹)	$\text{FWHM}(\text{[N II]})$ (km s ⁻¹)
(1)	(2)	(3)	(4)	(5)	(6)	(7)	(8)	(9)	(10)	(11)	(12)	(13)	(14)
NGC 185	<15.85	<15.85	<15.88	<15.88	-14.95	35	34.78	34.90	87
NGC 676	<18.91	<18.91	<18.77	<18.77	-21.49	172	39.04	38.62	264
NGC 777	20.88	21.18	21.02	21.44	8.5	2700	134	S	-21.94	...	<39.11	38.73	...
NGC 1058	<18.08	<18.08	<18.08	<18.08	-18.25	...	37.90	38.16	96
NGC 1068	22.11	22.59	22.49	22.98	18.5	1300	40	S+L ^a	-21.32	70	41.91	41.53	931
NGC 1167	23.46	23.67	23.78	23.97	8.5	2700	126	S	-21.31	70	40.76	40.81	550
NGC 1275	25.08	25.09	25.11	25.13	45.0	15000	170	U+L	-22.34	110	41.91	41.44	442
NGC 1358	20.62	21.56	20.78	21.79	33.0	8600	101	U+L	-20.95	165	40.67	40.19	246
NGC 1667	20.72	21.99	21.16	21.55	49.0	15000	0	U+D	-21.52	20	40.42	40.17	365
NGC 2273	21.14	21.41	21.45	21.71	6.0	830	42	S	-20.25	50	40.94	40.92	210
NGC 2639	22.57	22.60	22.23	22.35	<0.49	<100	...	U ^a	-20.96	140	40.40	40.48	401
NGC 2655	21.39	21.52	21.75	21.89	36.0	4300	108	U+L	-21.12	...	39.92	40.03	404
NGC 2685	<18.61	<18.61	<18.64	<18.64	-19.23	38	38.96	39.21	184
NGC 3031	19.30	19.34	19.21	19.29	45.0	300	45	U+L	-18.34	157	37.76	37.68	210
NGC 3079	21.66	21.97	21.57	22.14	46.4	4600	64	U+D	-21.14	165	40.21	41.03	900
NGC 3147	21.30	21.31	21.43	21.44	<0.45	<89	...	U	-21.82	155	40.07	40.01	427
NGC 3185	19.01	20.02	<18.94	<18.94	5.7	590	137	A	-18.99	130	39.90	40.07	232
NGC 3227	21.01	21.20	21.47	21.62	6.2	620	2	S	-20.39	155	40.51	40.20	471
NGC 3254	<18.90	<18.90	<18.90	<18.90	-20.35	46	39.34	39.16	155
NGC 3486	<17.90	<17.90	<17.90	<17.90	-18.58	80	37.99	37.85	149
NGC 3516	20.77	21.34	21.01	21.73	50.7	9600	38	S+L	-20.81	55	40.58	39.99	308
NGC 3735	20.21	20.40	20.20	20.51	<0.45	<89	...	U ^a	-21.62	131	40.60	40.55	274
NGC 3941	18.99	19.15	<18.78	<18.78	<0.53	<49	...	A	-20.13	10	39.01	39.16	273
NGC 3976	19.88	19.95	<19.49	<19.49	<0.66	<120	...	U	-21.28	53	39.48	39.57	279
NGC 3982	19.79	20.16	20.00	20.08	48.0	4000	10	U+D	-19.47	...	40.34	39.71	227
NGC 4051	19.87	20.54	20.17	20.69	15.1	1200	41	S+L	-20.41	135	39.81	39.68	228
NGC 4138	19.43	19.43	19.25	19.19	<0.51	<42	...	U	-19.05	150	38.92	38.71	211
NGC 4151	21.60	21.84	21.93	22.23	13.9	1400	82	S+L	-20.83	50	41.47	40.94	331
NGC 4168	20.23	20.24	20.13	20.18	<0.59	<48	...	U	-19.07	...	37.91	37.60	305
NGC 4169	19.76	20.28	19.80	20.43	3.5	860	110	A	-20.43	153	41.17	41.27	386
NGC 4235	20.87	20.93	20.70	20.91	<0.65	<110	...	U	-20.84	48	40.41	40.20	398
NGC 4258	18.99	19.29	18.98	19.64	0.80	26	149	S ^a	-20.63	150	39.02	38.60	296
NGC 4378	19.65	19.82	<19.25	<19.25	<0.62	<110	...	A	-20.51	167	39.01	38.95	340
NGC 4388	20.26	21.19	20.64	21.17	21.9	1800	14	S+L	-20.34	92	40.54	40.26	280
NGC 4395	18.02	18.29	18.38	18.49	<0.55	<10	...	U	-17.21	147	38.57	38.10	<123
NGC 4472	20.81	21.36	21.04	21.57	10.9	890	81	S	-21.80	...	<37.81	37.59	299
NGC 4477	18.76	18.94	<18.61	<18.61	<0.56	<46	...	A	-19.83	15	39.04	39.06	264
NGC 4501	19.55	19.55	19.79	19.84	<0.54	<44	...	U	-21.27	140	39.23	39.06	194
NGC 4565	19.47	19.48	19.36	19.48	<0.52	<25	...	U	-20.83	136	38.69	38.44	181
NGC 4579	21.11	21.16	20.80	20.98	6.2	510	133	U+L	-20.84	95	39.42	39.44	376
NGC 4639	18.87	19.30	<18.64	<18.64	<0.54	<44	...	A	-19.28	123	38.44	38.37	180
NGC 4698	18.94	19.02	<18.64	<18.64	<0.56	<46	...	A	-19.89	170	38.86	38.74	172
NGC 4725	<18.50	<18.50	<18.34	<18.34	-20.69	35	38.54	38.22	186
NGC 5033	20.10	21.00	20.38	20.83	40.0	3600	0	S+L	-21.15	170	39.72	39.70	261
NGC 5194	18.84	20.17	19.17	20.27	24.0	900	160	U+L	-20.76	163	39.83	39.80	224
NGC 5273	19.74	19.98	20.01	20.14	<0.52	<54	...	U	-19.26	10	39.25	38.70	147
NGC 5395	<19.70	<19.70	<19.59	<19.59	-21.34	167	39.14	39.35	187
NGC 5548	21.16	21.82	21.40	22.08	15.4	5000	163	U+L	-21.32	110	41.12	40.22	275
NGC 5631	19.68	19.58	19.57	19.74	<0.48	<76	...	A	-20.22	...	39.12	39.23	421
NGC 6951	19.85	19.93	20.21	20.41	<0.47	<55	...	U ^a	-21.20	170	40.11	40.49	232
NGC 7479	20.53	21.15	20.61	21.12	36.0	5700	0	U+L	-21.33	25	40.25	40.65	581
NGC 7743	20.30	20.33	20.38	20.59	1.29	150	33	S	-19.78	80	40.21	40.24	300

^aThe extended emission is not included in the morphological classification because it is thought to be associated with the host galaxy rather than the AGN.

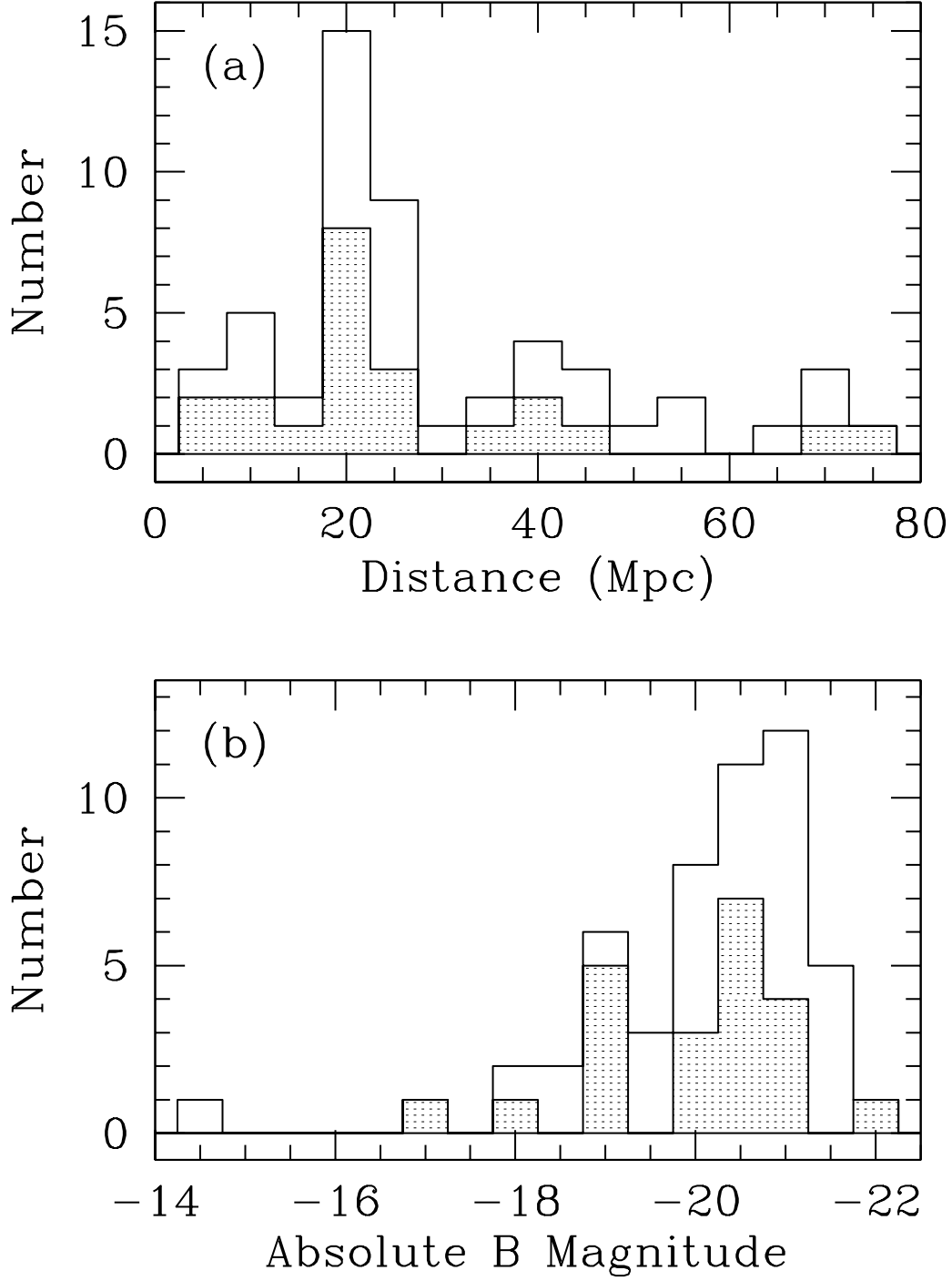


FIG. 1*a, b.*— Number distributions of (*a*) distance and (*b*) total absolute blue magnitude (corrected for internal extinction) for the Palomar Seyfert sample. The type 1 objects are shown as shaded histograms, and the total sample (types 1 and 2) is denoted by the unshaded histograms. All the data are taken from Ho et al. (1997a) and are given in Table 1.

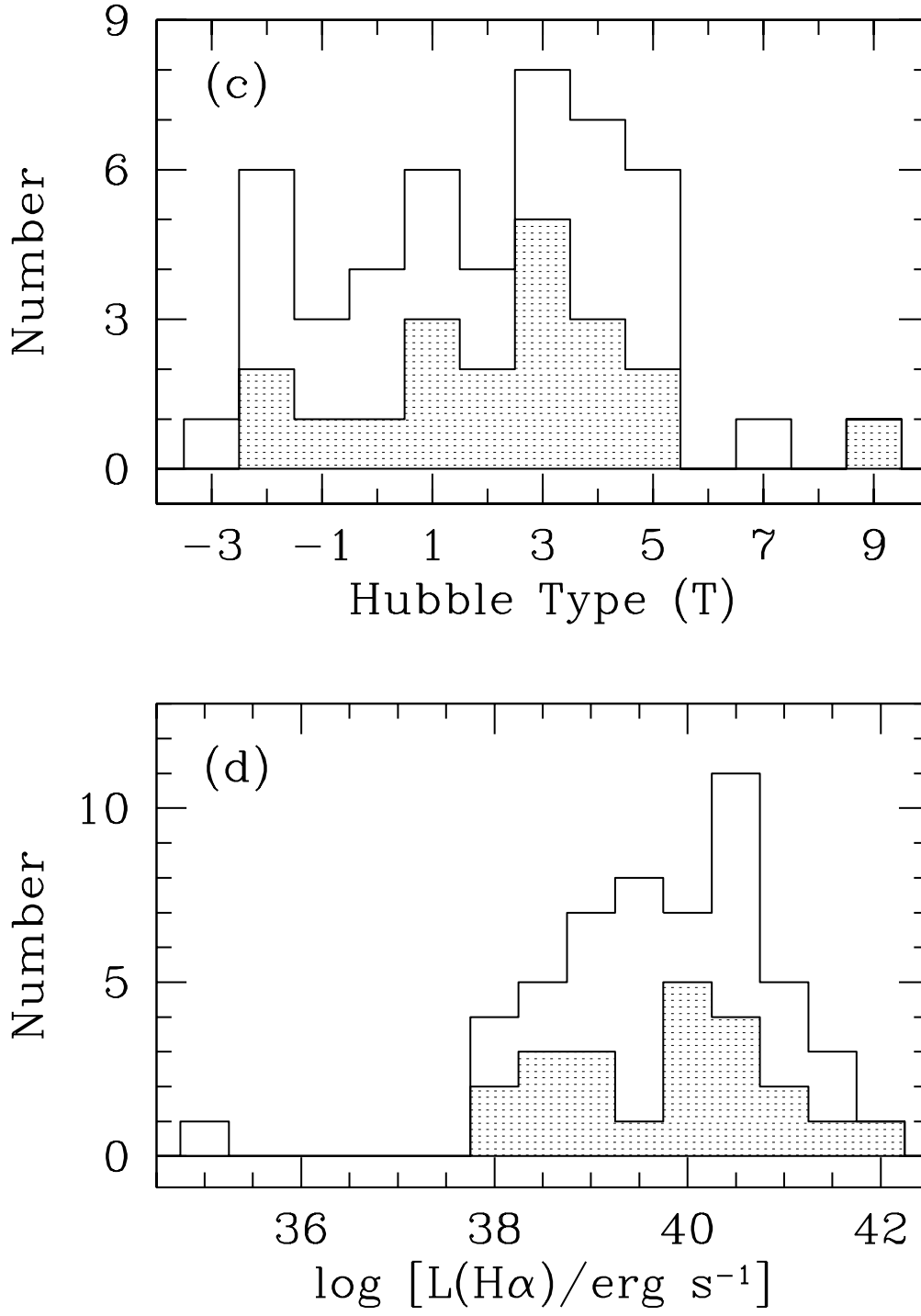


FIG. 1c, d.— Number distributions of (c) morphological type index, T (-3 to $-1 = S0$, $1 = Sa$, $3 = Sb$, $5 = Sc$, $7 = Sd$, $9 = Sm$) and (d) extinction-corrected luminosity of the narrow $H\alpha$ emission line for the Palomar Seyfert sample. The type 1 objects are shown as shaded histograms, and the total sample (types 1 and 2) is denoted by the unshaded histograms. All the data are taken from Ho et al. (1997a) and are given in Table 1.

Figure shown separately as JPEG image.

FIG. 2.— Full-resolution 20 cm (*a*) and 6 cm (*b*) and tapered 6 cm (*c*) maps of NGC 185, NGC 676, NGC 777, and NGC 1058.

Figure shown separately as JPEG image.

FIG. 3.— Full-resolution 20 cm (*a*) and 6 cm (*b*) and tapered 6 cm (*c*) maps of NGC 1068, NGC 1167, NGC 1275, and NGC 1358.

Figure shown separately as JPEG image.

FIG. 4.— Full-resolution 20 cm (*a*) and 6 cm (*b*) and tapered 6 cm (*c*) maps of NGC 1667, NGC 2273, NGC 2639, and NGC 2655. Panel (*c*) also shows the tapered 20 cm map of NGC 2655 (top).

Figure shown separately as JPEG image.

FIG. 5.— Full-resolution 20 cm (*a*) and 6 cm (*b*) and tapered 6 cm (*c*) maps of NGC 2685, NGC 3031, NGC 3079, and NGC 3147.

Figure shown separately as JPEG image.

FIG. 6.— Full-resolution 20 cm (*a*) and 6 cm (*b*) and tapered 6 cm (*c*) maps of NGC 3185, NGC 3227, NGC 3254, and NGC 3486.

Figure shown separately as JPEG image.

FIG. 7.— Full-resolution 20 cm (*a*) and 6 cm (*b*) and tapered 6 cm (*c*) maps of NGC 3516, NGC 3735, NGC 3941, and NGC 3976.

Figure shown separately as JPEG image.

FIG. 8.— Full-resolution 20 cm (*a*) and 6 cm (*b*) and tapered 6 cm (*c*) maps of NGC 3982, NGC 4051, NGC 4138, and NGC 4151.

Figure shown separately as JPEG image.

FIG. 9.— Full-resolution 20 cm (*a*) and 6 cm (*b*) and tapered 6 cm (*c*) maps of NGC 4168, NGC 4169, NGC 4203, and NGC 4235.

Figure shown separately as JPEG image.

FIG. 10.— Full-resolution 20 cm (*a*) and 6 cm (*b*) and tapered 6 cm (*c*) maps of NGC 4258, NGC 4378, NGC 4388, and NGC 4395.

Figure shown separately as JPEG image.

FIG. 11.— Full-resolution 20 cm (*a*) and 6 cm (*b*) and tapered 6 cm (*c*) maps of NGC 4450, NGC 4472, NGC 4477, and NGC 4501.

Figure shown separately as JPEG image.

FIG. 12.— Full-resolution 20 cm (*a*) and 6 cm (*b*) and tapered 6 cm (*c*) maps of NGC 4565, NGC 4579, NGC 4639, and NGC 4698.

Figure shown separately as JPEG image.

FIG. 13.— Full-resolution 20 cm (*a*) and 6 cm (*b*) and tapered 6 cm (*c*) maps of NGC 4725, NGC 5033, NGC 5194, and NGC 5273.

Figure shown separately as JPEG image.

FIG. 14.— Full-resolution 20 cm (*a*) and 6 cm (*b*) and tapered 6 cm (*c*) maps of NGC 5395, NGC 5548, NGC 5631, and NGC 6951.

Figure shown separately as JPEG image.

FIG. 15.— Full-resolution 20 cm (*a*) and 6 cm (*b*) and tapered 6 cm (*c*) maps of NGC 7479 and NGC 7743.

Figure shown separately as JPEG image.

FIG. 16*a, b.*— Objects with detected linear polarization. The contours show maps of total intensity, as in Fig. 2, and the vectors represent linearly-polarized emission.

Figure shown separately as JPEG image.

FIG. 16*c, d.*— Objects with detected linear polarization. The contours show maps of total intensity, as in Fig. 2, and the vectors represent linearly-polarized emission.

Figure shown separately as JPEG image.

FIG. 16*e, f, g.*— Objects with detected linear polarization. The contours show maps of total intensity, as in Fig. 2, and the vectors represent linearly-polarized emission.

Figure shown separately as JPEG image.

FIG. 16*h, i.*— Objects with detected linear polarization. The contours show maps of total intensity, as in Fig. 2, and the vectors represent linearly-polarized emission.

Figure shown separately as JPEG image.

FIG. 16*j, k.*— Objects with detected linear polarization. The contours show maps of total intensity, as in Fig. 2, and the vectors represent linearly-polarized emission.

Figure shown separately as JPEG image.

FIG. 16*l*.— Objects with detected linear polarization. The contours show maps of total intensity, as in Fig. 2, and the vectors represent linearly-polarized emission.

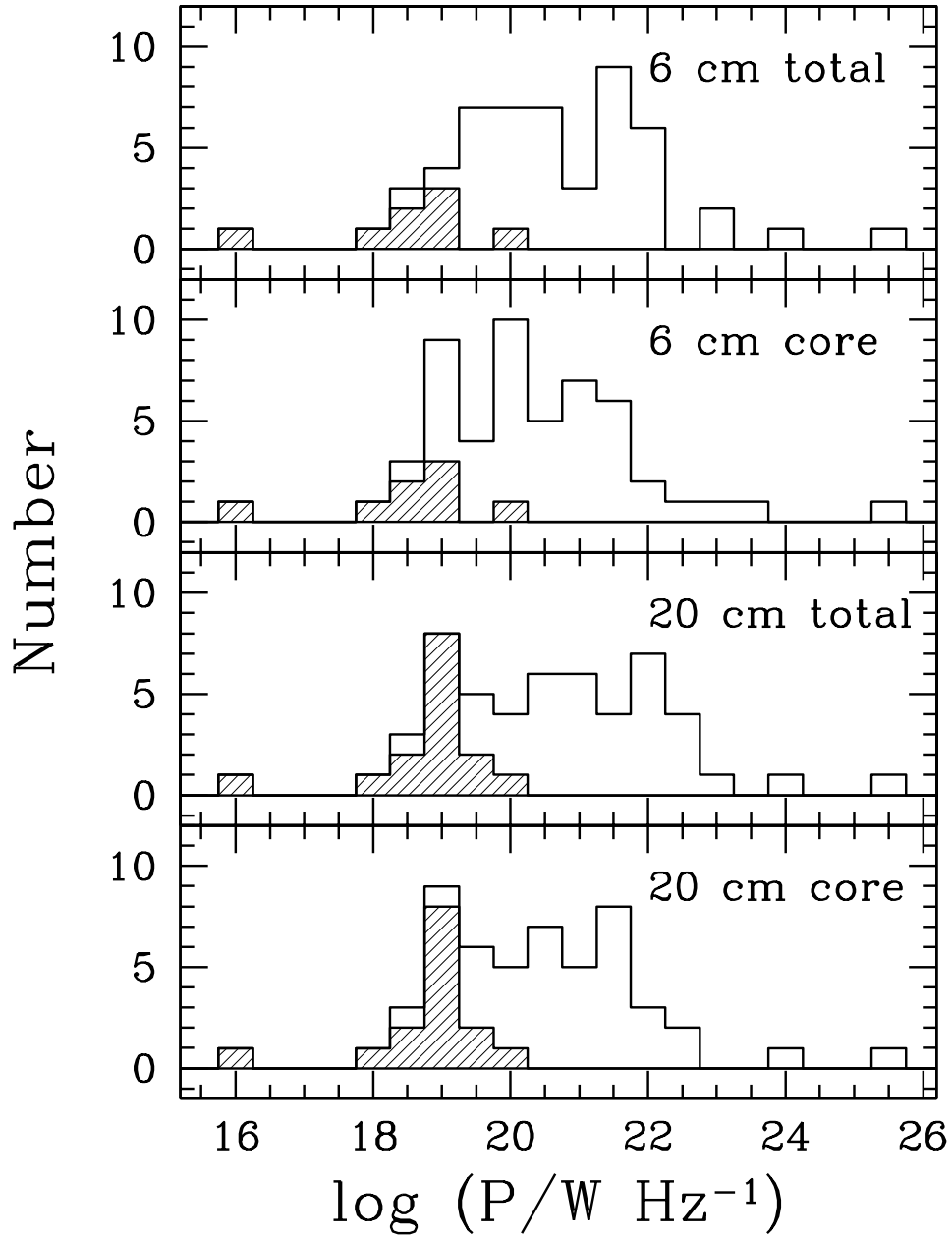


FIG. 17.— Number distributions of radio powers. The panels show, from top to bottom, measurements for the total integrated power at 6 cm, the peak core power at 6 cm, the total integrated power at 20 cm, and the peak core power at 20 cm. The shaded regions of the histogram denote upper limits.

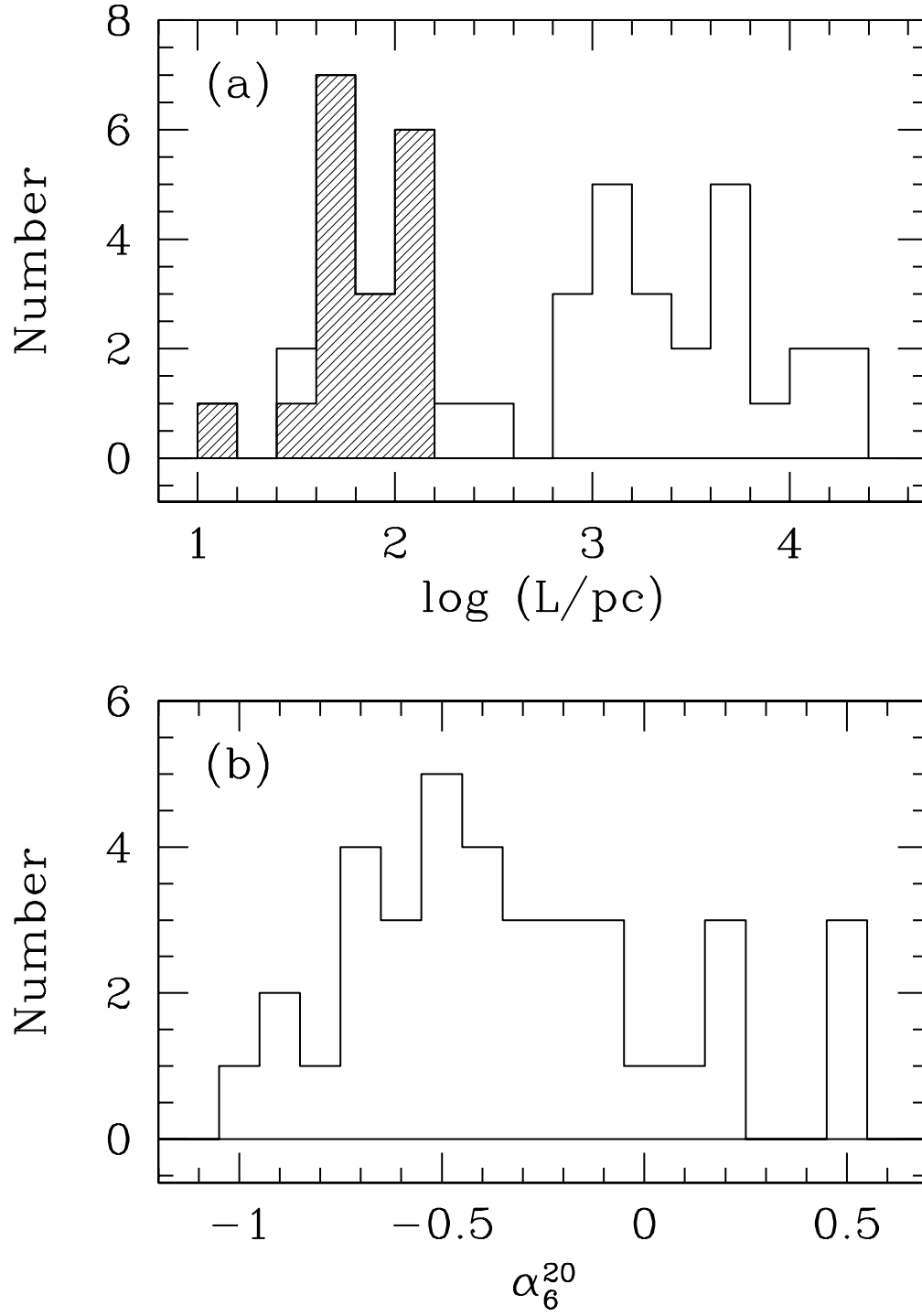


FIG. 18.— Number distributions of (a) linear source size and (b) spectral index between 6 and 20 cm. The shaded regions of the histogram denote upper limits.

This figure "fig16-p1.jpg" is available in "jpg" format from:

<http://arXiv.org/ps/astro-ph/0102506v1>

This figure "fig16-p2.jpg" is available in "jpg" format from:

<http://arXiv.org/ps/astro-ph/0102506v1>

This figure "fig2.jpg" is available in "jpg" format from:

<http://arXiv.org/ps/astro-ph/0102506v1>

This figure "fig16-p3.jpg" is available in "jpg" format from:

<http://arXiv.org/ps/astro-ph/0102506v1>

This figure "fig3.jpg" is available in "jpg" format from:

<http://arXiv.org/ps/astro-ph/0102506v1>

This figure "fig16-p4.jpg" is available in "jpg" format from:

<http://arXiv.org/ps/astro-ph/0102506v1>

This figure "fig4.jpg" is available in "jpg" format from:

<http://arXiv.org/ps/astro-ph/0102506v1>

This figure "fig16-p5.jpg" is available in "jpg" format from:

<http://arXiv.org/ps/astro-ph/0102506v1>

This figure "fig5.jpg" is available in "jpg" format from:

<http://arXiv.org/ps/astro-ph/0102506v1>

This figure "fig16-p6.jpg" is available in "jpg" format from:

<http://arXiv.org/ps/astro-ph/0102506v1>

This figure "fig6.jpg" is available in "jpg" format from:

<http://arXiv.org/ps/astro-ph/0102506v1>

This figure "fig7.jpg" is available in "jpg" format from:

<http://arXiv.org/ps/astro-ph/0102506v1>

This figure "fig8.jpg" is available in "jpg" format from:

<http://arXiv.org/ps/astro-ph/0102506v1>

This figure "fig9.jpg" is available in "jpg" format from:

<http://arXiv.org/ps/astro-ph/0102506v1>

This figure "fig10.jpg" is available in "jpg" format from:

<http://arXiv.org/ps/astro-ph/0102506v1>

This figure "fig11.jpg" is available in "jpg" format from:

<http://arXiv.org/ps/astro-ph/0102506v1>

This figure "fig12.jpg" is available in "jpg" format from:

<http://arXiv.org/ps/astro-ph/0102506v1>

This figure "fig13.jpg" is available in "jpg" format from:

<http://arXiv.org/ps/astro-ph/0102506v1>

This figure "fig14.jpg" is available in "jpg" format from:

<http://arXiv.org/ps/astro-ph/0102506v1>

This figure "fig15.jpg" is available in "jpg" format from:

<http://arXiv.org/ps/astro-ph/0102506v1>